Earth and Planetary Science Letters 319-320 (2012) 241–250

Contents lists available at SciVerse ScienceDirect

Earth and Planetary Science Letters

journal homepage: www.elsevier.com/locate/epsl

Constraints on the origin and relative timing of the Trezona $\delta^{13}C$ anomaly below the end-Cryogenian glaciation

Catherine V. Rose [a,*], Nicholas L. Swanson-Hysell [a], Jon M. Husson [a], Laura N. Poppick [a], John M. Cottle [b], Blair Schoene [a], Adam C. Maloof [a]

[a] Department of Geosciences, Princeton University, Guyot Hall, Washington Road, Princeton, NJ 08544, USA
[b] Department of Earth Science, University of California, Santa Barbara, CA 93106, USA

ARTICLE INFO

Article history:
Received 28 June 2011
Received in revised form 6 December 2011
Accepted 21 December 2011
Available online xxxx

Editor: G. Henderson

Keywords:
carbonates
carbon isotopes
diagenesis
Marinoan
Neoproterozoic
Trezona Formation

ABSTRACT

The Neoproterozoic Era was punctuated by the 'Sturtian' (~710 million years ago) and 'Marinoan' (~635 million years ago) low-latitude glaciations. Carbonates preceding the younger Marinoan glacial succession record an ~18‰ negative shift in the $\delta^{13}C$ of carbonate around the world. This 'Trezona' isotopic anomaly is the largest $\delta^{13}C$ shift in Earth history and its origin and timing remain controversial. The $\delta^{13}C$ anomaly could record a dramatic reorganization of Earth's carbon cycle and be linked causally to the initiation of Marinoan ice-house conditions. Alternatively, the $\delta^{13}C$ anomaly might record secondary fluid alteration following carbonate deposition. Here we document dropstones within the carbonate sediments immediately below the Marinoan glacial diamictite in South Australia. Advancing ice sheets caused soft-sediment deformation of the beds below the glacial diamictite, as well as subglacial erosion of the carbonates beneath, showing that the Trezona $\delta^{13}C$ values must have been acquired *before* glaciation. Although these stratigraphic relationships do not provide a specific mechanism to explain the Trezona $\delta^{13}C$ anomaly, they do require that the nadir of the Trezona $\delta^{13}C$ anomaly was recorded prior to local glacier advance and long before late-stage burial diagenesis could have occurred. Furthermore, the $\delta^{13}C$ recovery in the Trezona Formation toward 0‰ was synchronous with the appearance of icebergs in the tropics.

1. Introduction

Neoproterozoic carbonate carbon isotope records are characterized by two features unique to the era: 1) prolonged periods with high carbonate $\delta^{13}C$, and 2) short-term departures to negative $\delta^{13}C$ values. The Cryogenian (~710–635 Ma) $\delta^{13}C$ record exhibits increasing $\delta^{13}C$ after the Sturtian ice age, a +8‰ plateau, and finally an 18‰ negative shift in $\delta^{13}C$ preceding the Marinoan glaciation. This preglacial negative $\delta^{13}C$ 'Trezona' anomaly, named after its discovery in the Trezona Formation (Fm) of South Australia (McKirdy et al., 2001), gradually recovers from $\delta^{13}C$ of −10‰ towards 0‰ before the overlying glacial deposit. This trend likely represents a globally synchronous signal as it is recorded in carbonates on five continents (Halverson et al., 2005; Hoffman et al., 2002; Kaufman et al., 1997; McKirdy et al., 2001; Miller, 2008; Narbonne et al., 1994; Xiao et al., 2004) and always occurs stratigraphically above the +8‰ plateau and below the Marinoan glacial deposit. The glacial deposit has been correlated between continents using the overlying sedimentologically and geochemically distinct 'cap' carbonate sequences. An ash within the Marinoan glacial deposit in Namibia yielded an U–Pb age of 635.5 ± 0.6 Ma (Hoffmann et al., 2004), while an ash within the Marinoan cap carbonate in South China contained zircons dated at 635.2 ± 0.6 Ma using the U–Pb system (Condon et al., 2005). The Trezona $\delta^{13}C$ anomaly is comparable in magnitude to an anomaly that precedes the Sturtian glaciation on three cratons (>716.5 ± 0.24 Ma (Halverson et al., 2005; Macdonald et al., 2010)), as well as to the younger Shuram $\delta^{13}C$ excursion on five continents (full recovery dated at ~551 Ma, South China (Condon et al., 2005)) where $\delta^{13}C$ shifts from +4 to −12‰ before gradually recovering to positive values again (Burns and Matter, 1993; Calver, 2000; Kaufman et al., 2007; McFadden et al., 2008; Melezhik et al., 2008). Despite these similarities with the Trezona $\delta^{13}C$ anomaly, the goal of this paper is not to correlate the anomaly between continents or compare the $\delta^{13}C$ profile to other similar Neoproterozoic $\delta^{13}C$ anomalies. Instead, we document the Trezona $\delta^{13}C$ anomaly recorded on one continent across one basin and use stratigraphic relationships to evaluate the relative age of the $\delta^{13}C$ variability and glaciation.

The origin of such a large global isotopic shift remains contentious: does the anomaly represent a significant perturbation to the carbon cycle reflected in the global oceanic dissolved inorganic carbon (DIC) from which limestones are derived (Halverson et al., 2002; Pavlov et al., 2003; Schrag et al., 2002; Swanson-Hysell et al., 2010), or does it reflect diagenetic alteration of the limestones by porewaters (Derry, 2010a,b,c; Knauth and Kennedy, 2009; Swart and Kennedy, 2012)? Proponents of a primary DIC or early diagenesis origin interpret the close association of the Trezona $\delta^{13}C$ anomaly below M0arinoan glacial deposits

* Corresponding author. Tel.: +1 609 258 0836; fax: +1 609 258 1274.
E-mail address: cvrose@princeton.edu (C.V. Rose).

0012-821X/$ – see front matter © 2011 Elsevier B.V. All rights reserved.
doi:10.1016/j.epsl.2011.12.027

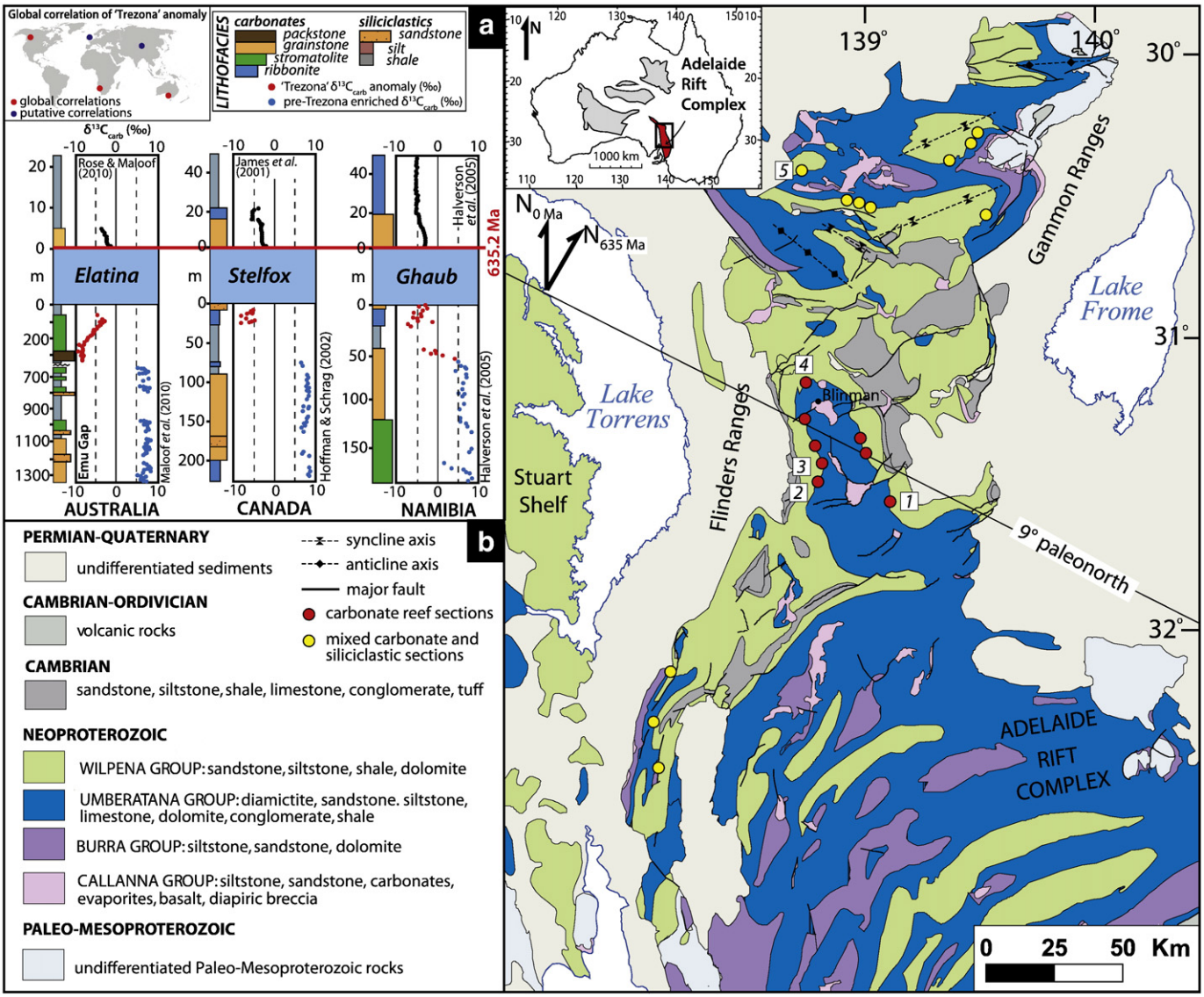

Fig. 1. (a) Inset: world map showing locations of Cryogenian interglacial successions that record the Trezona $\delta^{13}C$ anomaly: South Australia (McKirdy et al., 2001), northern Namibia (Halverson et al., 2005; Miller, 2008), northern Canadian cordillera (Hoffman et al., 2002; Kaufman et al., 1997; Narbonne et al., 1994), northwest China (Xiao et al., 2004), and Scotland (Prave et al., 2009). Simplified representative stratigraphic sections that record the large (~18‰) Trezona isotopic anomaly observed beneath the Elatina (Australia), Stelfox (Canada), and Ghaub (Namibia) glacial sediments. The Trezona anomaly recorded in limestones across the Adelaide Rift Complex (ARC), South Australia, is younger than a 659.7 Ma tuffaceous horizon in the Wilyerpa Fm (SHRIMP U–Pb zircon age), just above the Appila (Sturtian) diamictite (Fanning, 2006), and older than the ~635 Myr old Nuccaleena Fm 'cap dolostone', which has been correlated to U–Pb zircon-dated ashes within the Marinoan glacial deposit and cap dolostone in Namibia (Hoffmann et al., 2004) and China (Condon et al., 2005), respectively. (b) Inset: map illustrating the Neoproterozoic basins in Australia (gray) with the Adelaide Rift Complex (ARC) highlighted in red. Simplified geological map (adapted from Preiss and Robertson, 2002) of the study area within the ARC. Locations of measured stratigraphic sections are denoted by red dots (carbonate reef sections) and yellow dots (mixed carbonate-siliciclastic sections). Sections discussed in this paper are labeled with numbered squares (1. Emu Gap, 2. Elatina Creek, 3. Trezona Bore, 4. Mooloolo, and 5. Punches Rest). The orientation of paleonorth and paleolatitude depicted on the map are from paleomagnetic results measured in the Elatina Fm of the central Flinders Ranges (Sohl et al., 1999).

worldwide as evidence for a causal relationship between the two (Pavlov et al., 2003; Schrag et al., 2002; Swart and Kennedy, 2012). However, due to erosional unconformities truncating the upper recovering $\delta^{13}C$ trend (Halverson et al., 2002), no observation has constrained the timing of the Trezona $\delta^{13}C$ anomaly to the onset of the Marinoan glaciation.

There are five published hypotheses for the origin and timing of large-scale Neoproterozoic $\delta^{13}C$ excursions that can be applied to the Trezona $\delta^{13}C$ anomaly: (1) limestone $\delta^{13}C$ was reset during deep (>1 km) burial diagenesis by warm, CO_2-charged brines (Derry, 2010a,b; Grotzinger et al., 2011); (2) $\delta^{13}C$ records diagenetic alteration of shallowly-buried limestones associated with CO_2-charged brines rising from deeper overpressured reservoirs that were fractured during rapid deglacial sea level rise (Derry, 2010c); (3) $\delta^{13}C$ was altered during meteoric diagenesis and sea level drawdown during ice age initiation (Knauth and Kennedy, 2009; Swart and Kennedy, 2012); (4) $\delta^{13}C$ records changes in DIC either as a cause or consequence of the transition into a low-latitude glaciation (Pavlov et al., 2003; Schrag et al., 2002; Swanson-Hysell et al., 2010; Tziperman et al., 2011); and (5) $\delta^{13}C$ records primary changes in global oceanic DIC significantly before the onset of glaciation (Halverson et al., 2002).

The abundance of chemical sediments and broad range of pre- and syn-glacial paleo-environments and water depths across the Adelaide Rift Complex (ARC), South Australia, offer a unique opportunity to constrain the timing of the $\delta^{13}C$ anomaly relative to deposition of

the Trezona Fm and ensuing glaciation. In particular, the Trezona Fm includes outer shelf–slope stratigraphy that records continuous submarine deposition and $\delta^{13}C$ evolution while shallow carbonate platforms are subaerially exposed globally during glacial eustatic fall. Across the ARC, the Trezona Fm is preceded by the older Etina Fm and Enorama Fm and is overlain by the Elatina Fm. The Etina Fm consists of shallow marine sandstone, oolites and microbial reefs. The base of the Enorama Fm shale marks a major flooding surface, followed by a gradual coarsening and shoaling-upward sequence that culminates in intraclastic limestone breccias, stromatolite bioherms, oolitic grainstones and siltstones of the Trezona Fm. This carbonate succession consists of cm to m-scale parasequences that show no evidence of subaerial exposure. The Trezona Fm packstones contain putative skeletal fossil debris that onlap and drape the stromatolite bioherms and have been interpreted as the first sponge-grade metazoan body fossils (Maloof et al., 2010). Detailed mapping and 19 measured stratigraphic sections show that the pre- and syn-glacial facies record a progressive deepening towards the north of the ARC (Fig. 1). The pre-glacial Trezona Fm equivalent in the south is a thick, dark red, mud-cracked sandstone and siltstone deposit with medium-coarse grit lenses (Yaltipena Fm; Fig. 2b,c). These sediments inter-finger with nearshore channelized grainstones, stromatolite reefs, and limestone breccias in the central region (Fig. 2a), and transition to stormy outer shelf carbonate ribbonites and gray–green calcareous shales in the north. The overlying glacigenic Elatina Fm transitions from marine sands in the south, to ice-contact tillites in the central region (Fig. 2g,h), and debris flows and turbidites in the north. In this paper, we present paired sedimentological and geochemical evidence from the ARC that constrain the recovery from the Trezona $\delta^{13}C$ isotopic nadir to be synchronous with the appearance of icebergs in the tropics. These new observations constrain the timing of the $\delta^{13}C$ trend, and thus, rule out hypotheses 1, 2 and 5, and allow us to evaluate hypotheses 3 and 4 for the origin of the Trezona $\delta^{13}C$ anomaly.

2. Methods

2.1. $\delta^{13}C$ methods

Carbonates were sampled at ~1.0 m resolution whilst measuring 5 stratigraphic sections from across the ARC. Clean dolostones and limestones without siliciclastic components, secondary veining or cleavage were targeted. A total of 1042 samples were slabbed and polished perpendicular to bedding and 5 mg of powder were micro-drilled from individual laminations for isotopic analysis. At the University of Michigan Stable Isotope Laboratory, all powders were heated to 200 °C to remove volatile contaminants and water. Samples were then placed in individual borosilicate reaction vessels and reacted at 76 °C with 3 drops of H_3PO_4 in a Finnigan MAT Kiel I preparation device coupled directly to the inlet of a Finnigan MAT 251 triple collector isotope ratio mass spectrometer. $\delta^{13}C$ and $\delta^{18}O$ data were acquired simultaneously and are reported in the standard delta notation as the ‰ difference from the VPDB standard. Measured precision was maintained at better than 0.1‰ (1σ) for both $\delta^{13}C$ and $\delta^{18}O$. At Princeton University, all carbonate powders were heated to 110 °C to remove water. Samples were then placed in individual borosilicate reaction viles and reacted at 72 °C with 5 drops of H_3PO_4 in a GasBench II preparation device coupled directly to the inlet of a Thermo DeltaPlus continuous flow isotope ratio mass spectrometer. $\delta^{13}C$ and $\delta^{18}O$ data were acquired simultaneously and are reported in the

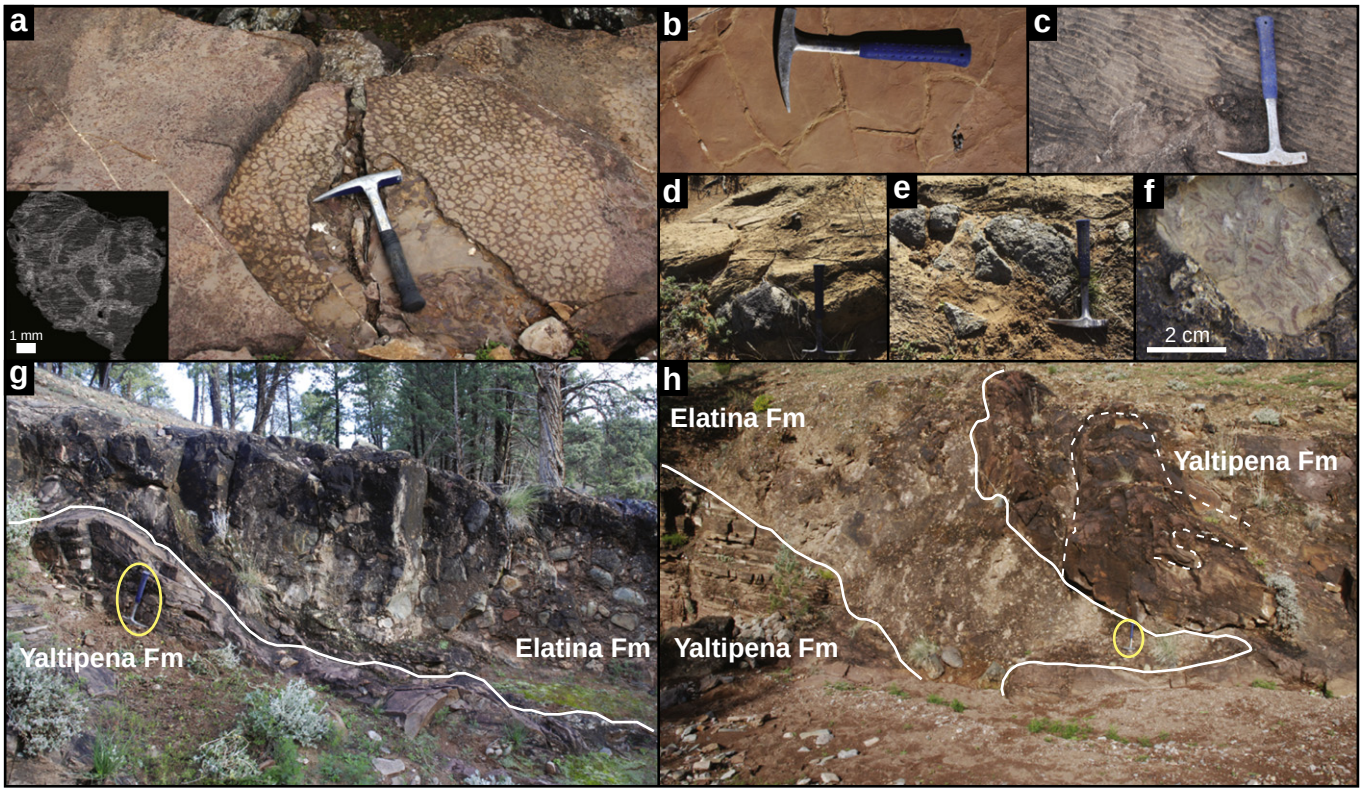

Fig. 2. (a) Outcrop of the Trezona Fm showing putative skeletal morphologies in fossil debris onlapping and draping a stromatolite bioherm (under the 30 cm long hammer) (Maloof et al., 2010). A 3D reconstruction of one such fossil is shown in the inset image. (b–c) Mudcracked siltstone and symmetric micro-wave ripples, Yaltipena Fm at Trezona Bore (Section [3], Figs. 1b and 3a), indicating intermittent subaerial exposure and very shallow water respectively. (d–e) Granitoid clasts within microbialite bioherm of the Trezona Fm at Punches Rest (Section [5], Figs. 1b and 3a). (f) Trezona Fm fossiliferous packstone clast within the glacial diamictite of the Elatina Fm. (g) Elatina Fm diamictite resting unconformably on tidal flat sandstone of the Yaltipena Fm as a result of ice-contact deposition, Trezona Bore. (h) Sub-glacial push structure lying unconformably on the Yaltipena Fm (right of image) at Trezona Bore. Note hammer for scale. The scoured basal contact and contorted diamictite beds indicate local ice-contact deposition and sub-glacial push structures.

standard delta notation as the ‰ difference from the VPDB standard. Precision and accuracy of data are monitored through analysis of 21 standards which are run for every 59 samples. Measured precision is maintained at better than 0.1‰ (1σ) for both $\delta^{13}C$ and $\delta^{18}O$.

2.2. Geochronology methods

Zircon separates were prepared using standard crushing, heavy liquid, and isodynamic separation techniques. To minimize any potential sampling bias, an aliquot of between 500 and >2000 zircons from the bulk separate were mounted (without hand picking) directly into a 25 mm diameter epoxy resin disc and polished. All zircons were mapped using a cathodoluminescence imaging system attached to a FEI Q400 FEG scanning electron microscope (SEM) housed at the University of California, Santa Barbara. The SEM was operated at 10 kV accelerating voltage and a beam current of 0.5 nA. The cathodoluminescence images revealed simple concentric zonation in the majority of zircons that were targeted (Fig. S1).

Zircons were analyzed for U, Th and Pb isotopes using a Laser Ablation Multi-Collector Inductively Coupled Plasma Mass Spectrometer (LA-MC-ICPMS) system housed at the University of California, Santa Barbara. Instrumentation consists of a Nu Plasma MC-ICP-MS (Nu Instruments, Wrexham, UK) and a 193 nm ArF laser ablation system (Photon Machines, San Diego, USA). Analytical protocol is similar to that described by (Cottle et al., 2009a, b, c). U–Th–Pb analyses were conducted for 15 s each using a spot diameter of 24 μm, a frequency of 4 Hz and 1.2 J/cm^2 fluence (equating to crater depths of approximately 4 μm). U–Th–Pb data from 5 samples were collected over 4 days of continuous instrument operation. A primary reference material, '91500' zircon (1065.4 ± 0.6 Ma $^{207}Pb/^{206}Pb$ ID-TIMS age and 1062.4 ± 0.8 Ma $^{206}Pb/^{238}U$ ID-TIMS age (Wiedenbeck et al., 1995)) was employed to monitor and correct for mass bias as well as Pb/U and fractionation. To monitor data accuracy, a secondary reference zircon 'GJ-1' (608.5 ± 0.4 Ma $^{207}Pb/^{206}Pb$ ID-TIMS

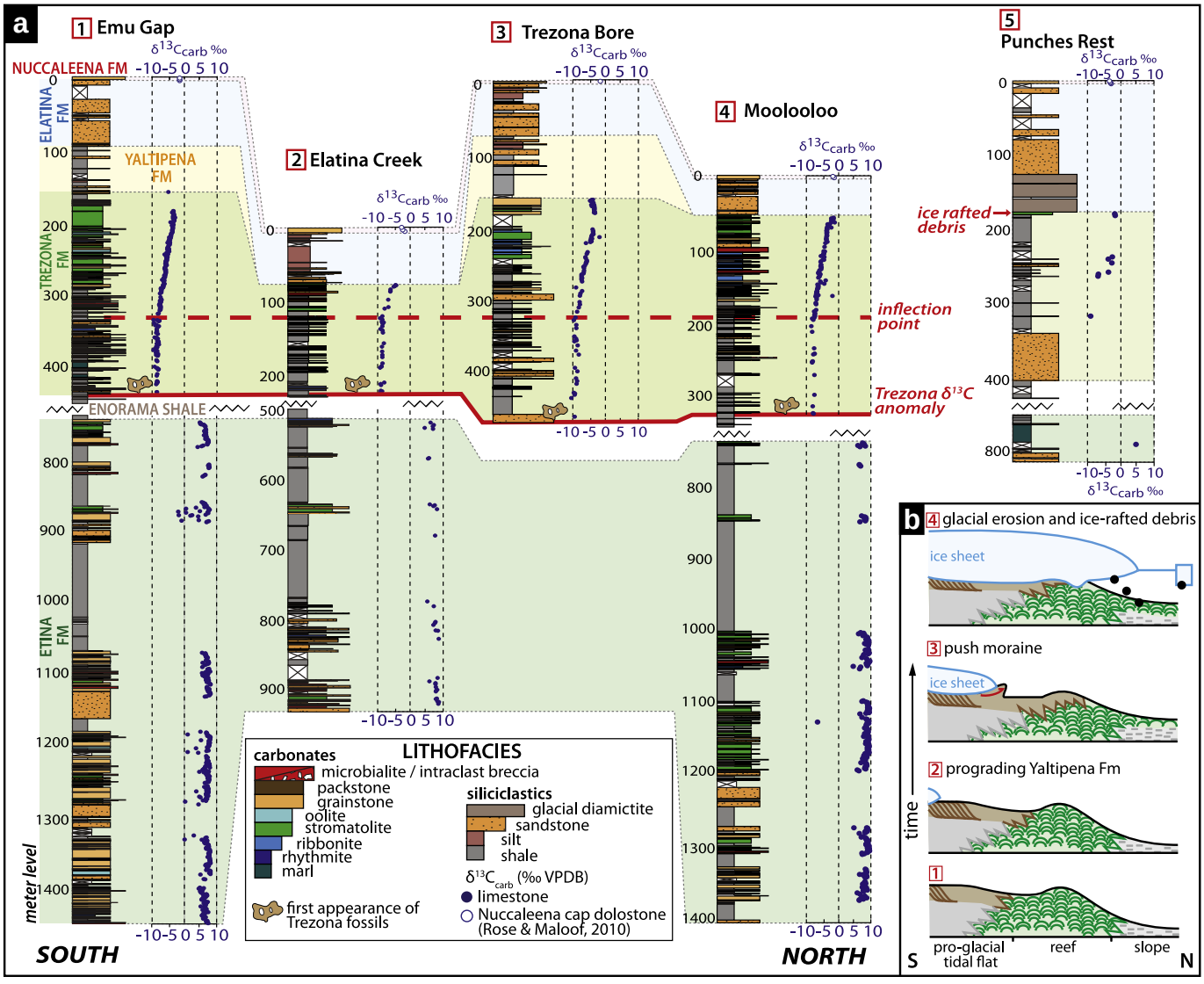

Fig. 3. (a) Selection of stratigraphic sections from the central anticline of the ARC (numbered to correspond with Fig. 1). The stratigraphic sections were drafted using MatStrat software (Lewis et al., 2011). Pre-glacial $\delta^{13}C$ data within the Etina and Trezona Fms are denoted by blue circles and $\delta^{13}C$ data within the post-glacial Nuccaleena Fm cap dolostone are denoted by white circles (Rose and Maloof, 2010). All sections are hung from a datum chosen at the inflection point at the base of the recovery from the Trezona negative $\delta^{13}C$ anomaly. The Yaltipena Fm progressively thins until it is missing entirely at the Elatina Creek section (Elatina Creek, [2]). Differential glacial erosion truncated the Yaltipena Fm during the ice advance. Furthermore, the $\delta^{13}C$ data indicate truncation of the Trezona Fm's reproducible carbon isotopic trend, thereby quantifying the degree and lateral variability of glacial erosion. Note that the Enorama Fm consists of shale with no associated $\delta^{13}C$ data and therefore has been omitted from the stratigraphic sections for clarity. (b) Schematic depositional model for the central anticline and northern region of the ARC, showing ice-contact deformation of the Yaltipena Fm and glacial truncation of the Trezona Fm in the central fold, and synchronous deposition of dropstones within stromatolites in the uppermost Trezona Fm to the north.

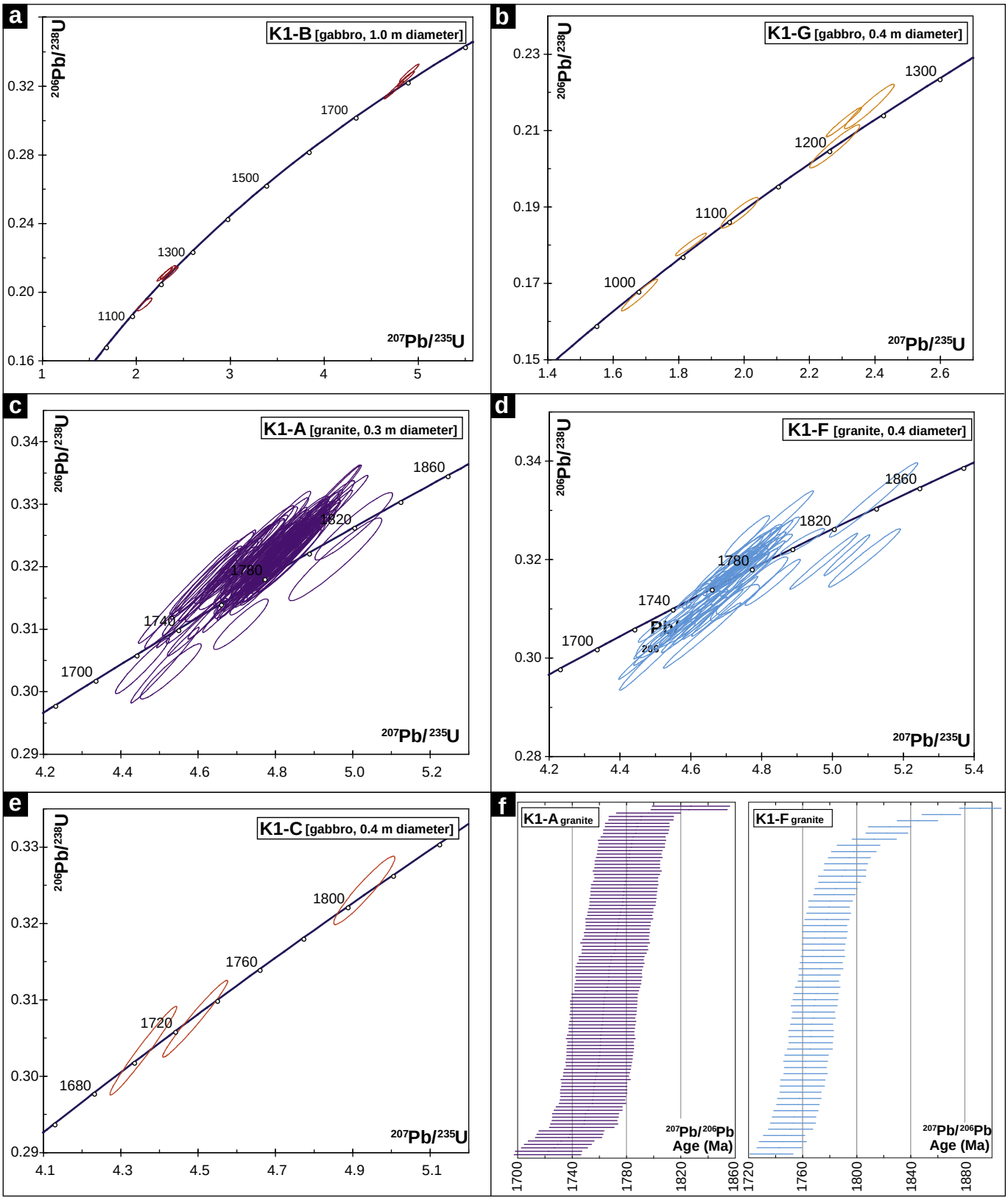

Fig. 4. U–Pb concordia diagrams for five ice-rafted clasts in the top of the Trezona Fm carbonate platform. We interpret the average of the concordant zircons to approximate the crystallization age of the clast. (a–b) Two gabbro clasts (K1–B and K1–G) are ~1000 Ma and ~1140 Ma, whilst two granite clasts (K1–A and K1–F) and a gabbro clast (K1–C) record ~1780 Ma and ~1700 Ma crystallization ages, respectively (c–e). These ages all can be derived from west and north regions of the Australian continent, respectively. (f) $^{207}Pb/^{206}Pb$ dates for single-grain zircons from granite clasts, color-coded to samples in c and d. All uncertainties are 2σ.

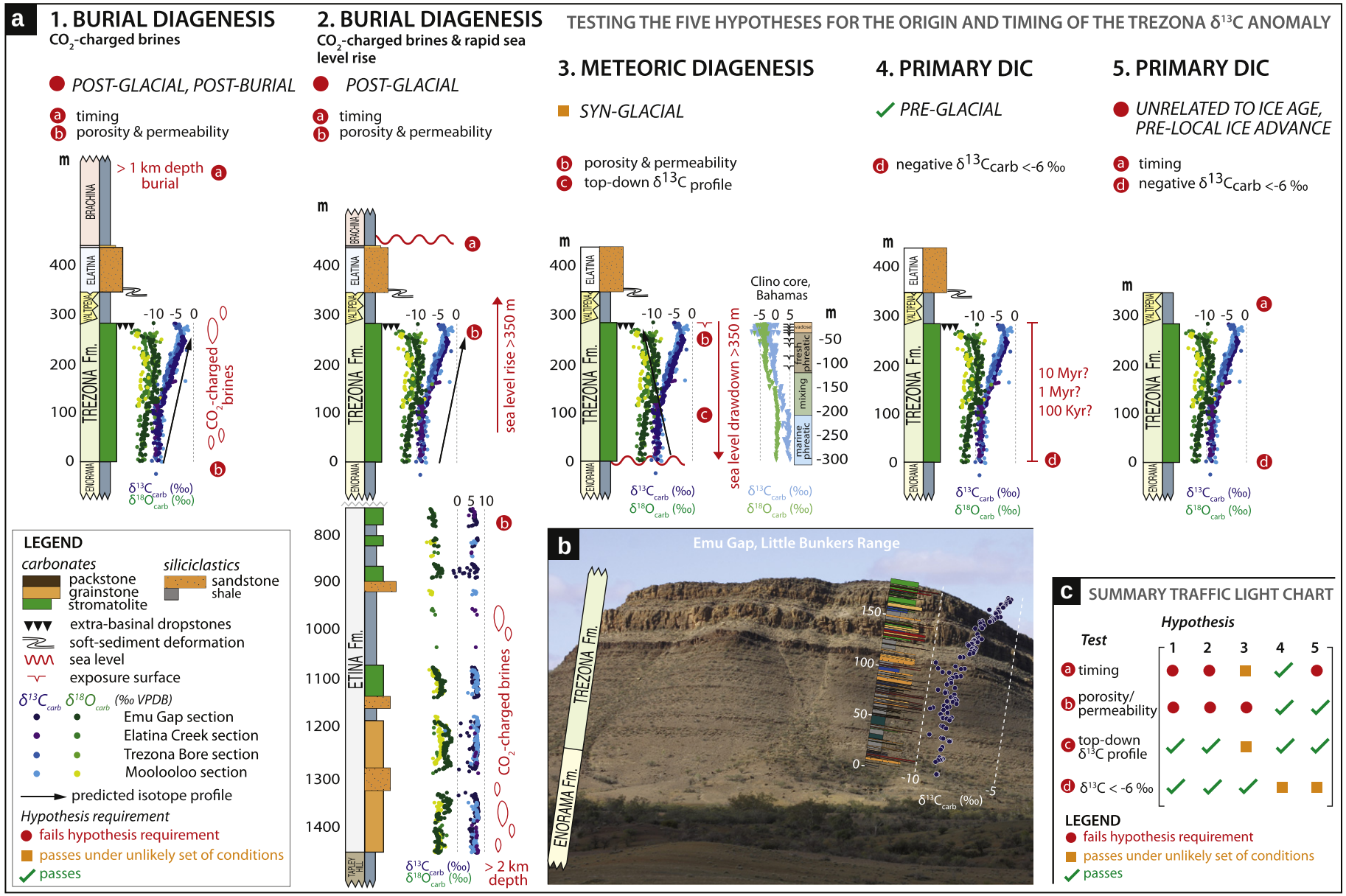
a
1. BURIAL DIAGENESIS
CO2-charged brines
POST-GLACIAL, POST-BURIAL
a timing
b porosity & permeability
> 1 km depth burial
CO2-charged brines
2. BURIAL DIAGENESIS
CO2-charged brines & rapid sea level rise
POST-GLACIAL
a timing
b porosity & permeability
sea level rise >350 m
TESTING THE FIVE HYPOTHESES FOR THE ORIGIN AND TIMING OF THE TREZONA δ13C ANOMALY
3. METEORIC DIAGENESIS
SYN-GLACIAL
b porosity & permeability
c top-down δ13C profile
sea level drawdown >350 m
Clino core, Bahamas
vadose
fresh phreatic
mixing
marine phreatic
4. PRIMARY DIC
PRE-GLACIAL
d negative δ13Ccarb <-6 ‰
10 Myr?
1 Myr?
100 Kyr?
5. PRIMARY DIC
UNRELATED TO ICE AGE, PRE-LOCAL ICE ADVANCE
a timing
d negative δ13Ccarb <-6 ‰
BRACHINA
ELATINA
WALTEMA
TREZONA Fm.
ENORAMA
ETINA Fm.
TARCEY HILL
δ13Ccarb (‰)
δ18Ocarb (‰)
> 2 km depth
LEGEND
carbonates
packstone
grainstone
stromatolite
siliciclastics
sandstone
shale
extra-basinal dropstones
soft-sediment deformation
sea level
exposure surface
δ13Ccarb δ18Ocarb (‰ VPDB)
Emu Gap section
Elatina Creek section
Trezona Bore section
Mooloolo section
predicted isotope profile
Hypothesis requirement
fails hypothesis requirement
passes under unlikely set of conditions
passes
b
Emu Gap, Little Bunkers Range
c
SUMMARY TRAFFIC LIGHT CHART
Hypothesis
Test
1 2 3 4 5
a timing
b porosity/ permeability
c top-down δ13C profile
d δ13C < -6 ‰
LEGEND
fails hypothesis requirement
passes under unlikely set of conditions
passes

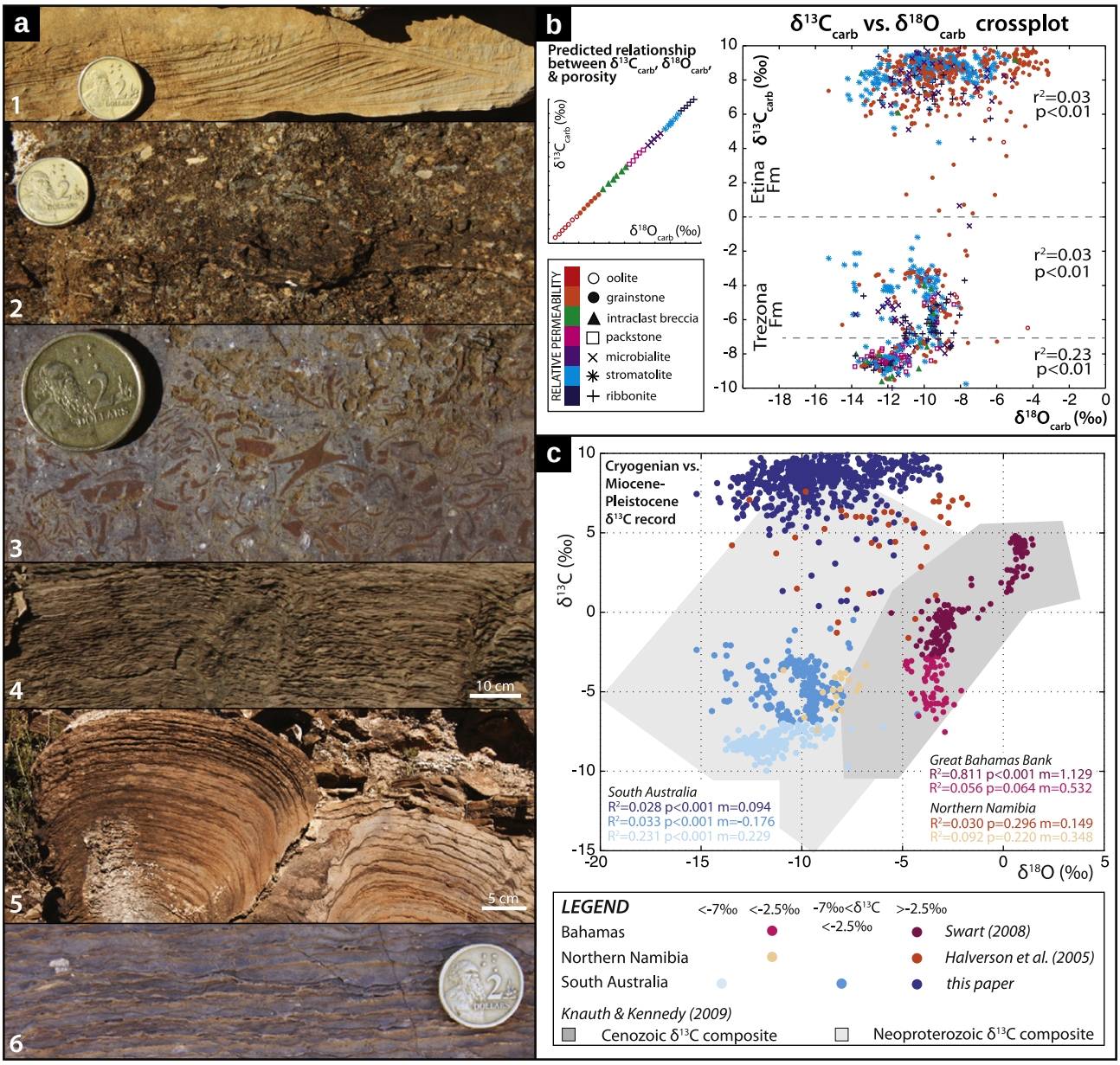

Fig. 6. (a) Field photos showing the predominant lithofacies within the Trezona Fm: (1) grainstone; (2) intraclast breccia; (3) packstone; (4) microbialite; (5) stromatolite; and (6) ribbonite. Diameter of coin is 20.5 mm. (b) Crossplot showing $\delta^{18}O$ vs. $\delta^{13}C$ data for the Trezona and Etina Fms from the Emu Gap, Elatina Creek, Trezona Bore, and Mooloolo sections with data color-coded by facies and relative permeability (Figs. 1b and 3a [1–4]. If diagenetic fluid-rock interactions control the $\delta^{13}C$–$\delta^{18}O$ in the Trezona Fm, $\delta^{13}C$ and $\delta^{18}O$ should be most negative in the most permeable sediments, and should become less altered (although not necessarily with a linear relationship) in less permeable units. (c) A crossplot comparing $\delta^{18}O$–$\delta^{13}C$ for the Cryogenian 'Trezona' $\delta^{13}C$ anomaly in South Australia (this paper) and northern Namibia (Halverson et al., 2005), and the Miocene–Pleistocene Clino core record, Great Bahamas Bank (Swart, 2008). Light colors represent $\delta^{13}C$ <−2.5‰ and dark colors for $\delta^{13}C$ >−2.5‰. The Trezona Fm (South Australia) is further divided into $\delta^{13}C$ <−7.0% (pale blue) and $\delta^{13}C$ >−7.0‰ (mid blue). The dark and light gray shaded regions represent Cenozoic and Neoproterozoic $\delta^{18}O$–$\delta^{13}C$ data composites, respectively (Knauth and Kennedy, 2009). (For interpretation of the references to color in this figure legend, the reader is referred to the web version of this article.)

age (Jackson et al., 2004) and 601.7 ± 1.3 Ma $^{206}Pb/^{238}U$ ID-TIMS age) was analyzed concurrently (once every 5–7 unknowns) and mass bias- and fractionation-corrected based on measured isotopic ratios of the primary reference material. Analyses of the GJ-1 secondary reference zircon during the analytical period yield a weighted mean $^{206}Pb/^{238}U$ age of 603.9 ± 0.6 Ma, MSWD = 0.9. Data reduction, including corrections for

Fig. 5. (a) Schematic diagram illustrating the five hypotheses for the origin and timing of the Trezona $\delta^{13}C$ anomaly. Hypotheses 1–2 propose that late-stage burial diagenesis generated CO_2-charged brines that reset the $\delta^{13}C$ values (Derry, 2010a; Derry, 2010b; Derry, 2010c; Grotzinger et al., 2011). Hypothesis 3 proposes that $\delta^{13}C$ values were altered during early meteoric diagenesis associated with glacio-eustatic sea level drawdown (Knauth and Kennedy, 2009; Swart and Kennedy, 2012). Data from the Clino core of the Great Bahama Banks provides a modern analog of a carbonate platform that has experienced pervasive meteoric diagenesis (Swart, 2008). Note that the recovery from the nadir of the Trezona $\delta^{13}C$ anomaly toward positive $\delta^{13}C$ values spans hundreds of meters (except where truncated) and is restricted to beneath the glacial surface. In contrast, the thin layer of positive $\delta^{13}C$ values at the top of Clino core and other Plio-Pleistocene cores are recorded within the post-glacial Holocene (Swart and Kennedy, 2012). Hypotheses 4–5 suggest that the $\delta^{13}C$ values record primary changes in DIC, either as a cause, consequence, or coincidental with the transition into a low-latitude glaciation (Halverson et al., 2002; Pavlov et al., 2003; Schrag et al., 2002; Swanson-Hysell et al., 2010). The problems with each hypothesis are highlighted by red circles labeled a–d and are referred to in the main text. The Trezona $\delta^{13}C$ data are from the four measured sections in the central Flinders region overlain on each other, illustrating the reproducibility across the ARC. (b) Laterally continuous outcrop of a stromatolite reef within the Trezona Fm exposed along the Little Bunkers Range (Fig. 1b [1]). The detailed Emu Gap stratigraphic section and associated $\delta^{13}C$ isotope data are overlaying the outcrop (Fig. 3a [1]). (c) A summary traffic light matrix illustrating which of the five hypotheses fail the fewest tests.

baseline, instrumental drift, mass bias, down-hole fractionation and age calculations was carried out using Iolite version 2.1.2 (Paton et al., 2010). All reported uncertainties are quoted at the 95% confidence or 2σ level and include contributions from the external reproducibility of the primary reference material for the $^{207}Pb/^{206}Pb$ and $^{206}Pb/^{238}U$ ratios. The complete dataset is presented in SOM, Table 2.

3. Results

Five new field observations constrain the origin and timing of the Trezona anomaly as a signal that was recorded in carbonates prior to burial, and whose recovery was concurrent with the onset of the ice age. *First*, in the northern ARC, isolated rounded ~0.2–1.0 m diameter granite and gabbro clasts are incorporated within the upper 2 m of a Trezona Fm stromatolite bioherm that records the highest $\delta^{13}C$ following the Trezona anomaly (Punches Rest; Fig. 2d, e and 3a [5]). This ice-rafted debris requires overlying icebergs in water possibly no deeper than the photic zone during terminal carbonate deposition on the outer shelf. The boulder horizon probably does not represent a debris flow sourced from an active salt diapir (Lemon, 2000) because: (1) three sections measured along the Punches Rest syncline show that this boulder horizon is the only one within the ~300 m thick Trezona Fm; (2) the single horizon occurs <2 m below the first Elatina Fm diamictites that contain similar boulders; (3) microbialite growth around the clasts appears continuous, without evidence of a high-energy erosion surface or winnowing of any associated finer debris; and (4) in map view, the nearest diapir cross-cuts the Etina Fm but only impinges on the lowermost ~50 m of the Trezona Fm, ~5 km south of the horizon. This observation suggests that during the deposition of the upper Trezona Fm and Elatina Fm, the nearby diapirs were not emergent or obviously active. However, some of the clasts within the horizon may have originated from a more distal diapir that was eroded and transported by the ice sheet.

Zircons from five of the ice-rafted clasts were dated by U–Pb LA-ICPMS to constrain the source of the debris (Fig. 4). Two gabbro clasts contain ~1000–1140 Ma igneous zircons, consistent with an Australian intra-continental source in the Musgrave Block, Northampton Inlier and/or Albany-Frazier Province (Fig. 4a, b). Similarly, granite and gabbro clasts with ~1780 Ma crystallization ages may have been sourced from the Mt. Painter Block, Stuart Shelf basement and/or Peak and Denison Inliers (Fig. 4c–e). Alternatively, these clasts could originate from the Grenville and Yavapai–Mazatzal provinces, respectively, of Laurentia and/or East Antarctica that abutted Australia for the previous 300 My (Karlstrom and Bowring, 1988; Goodge et al., 2008). The m-scale diameter of some boulders is consistent with an intra-continental origin, with ice potentially covering at least the southern half of Australia. However, the Li et al. (2008) paleogeographic reconstruction of the break up of Rodinia does not exclude the clasts being debris delivered to the tropics by sea ice prior to substantial ice sheet growth, sea level fall, and subaerial exposure of the Trezona Fm.

Together, the remaining field observations constrain the Trezona anomaly to be a syn-depositional $\delta^{13}C$ signal recorded in carbonates. *Second*, a scoured basal contact and contorted diamictite beds at the base of the Elatina Fm at the Trezona Bore section (Fig. 3a [3]) indicate local ice-contact and sub-glacial push structures formed during an ice advance (Lemon and Gostin, 1990) (Fig. 2g, h). Associated soft-sediment deformation of the Yaltipena Fm silts below the diamictite suggests the silts were unlithified and were rucked up during glaciation by overriding ice, and that even the basal Trezona Fm was only shallowly (<300 m) buried. *Third*, local glacial erosion variably truncates the Yaltipena Fm, such that this formation is entirely missing in parts of the central Flinders anticline (Fig. 3a [2], [4]). *Fourth*, local glacial erosion also truncates the carbon isotope records in the Trezona Fm across the ARC. All stratigraphic sections across the ARC show a dramatic shift in $\delta^{13}C$ from +9‰ to −9‰ within the Enorama Fm, before recovering towards 0‰ within the overlying Trezona Fm. The upper ~15 m of the Trezona Fm typically record a ~1‰ decline in $\delta^{13}C$, with an increase in scatter and a decrease in mean $\delta^{18}O$ values. However, these characteristics are truncated in the Elatina Creek and Mooloolloo sections, where the advancing ice incised through the Yaltipena Fm into the Trezona Fm (Fig. 3a [2], [4]). *Fifth*, ~20 cm sub-angular limestone packstone clasts of the Trezona Fm, which contain the distinctive skeletal fossil debris (Maloof et al., 2010), are present as clasts within the Elatina Fm diamictite near Punches Rest (Fig. 2f and 3a [5]). Observations 3–5 indicate that differential glacial erosion removed the unlithified Yaltipena Fm and locally incised the carbonate platform at least 150 m during ice advance. Collectively, all five new observations support the idea that deposition of the upper Trezona Fm and recovery from the 18‰ $\delta^{13}C$ anomaly were contemporaneous with local glaciation. In light of the new sedimentological and geochemical evidence from the ARC, we evaluate the five published hypotheses for the origin and timing of the Trezona $\delta^{13}C$ anomaly.

4. Discussion

4.1. Post-glacial burial diagenesis

High-temperature (>100 °C) fluid–rock interactions during burial are a potential secondary diagenetic origin for highly negative and co-varying carbonate $\delta^{13}C$ and $\delta^{18}O$ (Derry, 2010a,b,c) (Hypotheses 1 and 2) (Fig. 5a [1], [2]). A recent hypothesis suggests that the Ediacaran-age Shuram $\delta^{13}C$ anomaly and covarying $\delta^{13}C$–$\delta^{18}O$ can be explained with a two component mixing model combining high pCO_2, low $\delta^{13}C$ fluid developed from interaction with organic matter at depth, and high $\delta^{18}O$ basinal brine (Derry, 2010a,b,c). Minimal $\delta^{13}C$–$\delta^{18}O$ covariation occurs within the carbonate grainstones of the Etina Fm that underlie the Enorama Fm ($r^2 = 0.03$, $p < 0.01$) (Fig. 6a–c). $\delta^{13}C$–$\delta^{18}O$ covariation within the Trezona Fm is restricted to $\delta^{13}C$ values <−7‰ in the lowermost ~150 m of the Trezona anomaly within individual sections and is of unknown origin (Fig. 6b, c). However, geological observations 1–5 are inconsistent with a burial diagenetic origin for the Trezona $\delta^{13}C$ anomaly because the $\delta^{13}C$ signal must have been recorded in sediment prior to glaciation.

Any burial diagenesis hypothesis requires that organic-rich sediments reach temperatures >60 °C for thermal cracking reactions to generate hydrocarbons and release CO_2-rich fluids that alter overlying carbonates during upward fluid migration (Seewald, 2003). Hypothesis 1 proposes that additional sedimentary overburden above the Trezona Fm helped generate such CO_2-charged brines (Fig. 5a [1]). Hypothesis 2 also calls upon hydrocarbon migration, but suggests that ^{13}C-depleted brines were released during post-glacial sea level rise when hydrostatic over-pressure caused the reservoir seal to fracture, leading to a global diagenesis event (Derry, 2010c) (Fig. 5a [2]). The Enorama Fm shale underlying the Trezona Fm is the only viable source of ^{13}C-depleted carbon, since the very permeable Etina Fm grainstones below remain at +10‰ (Fig. 5a [1]). Hypotheses 1 and 2 demand that the Trezona $\delta^{13}C$ anomaly was recorded diagenetically either after the glaciation, or after burial under >1 km of overlying sediments. However, the Trezona $\delta^{13}C$ anomaly and the then unlithified Yaltipena Fm are variably truncated across the carbonate platform, indicating that the isotope signature was acquired in the carbonates before interfingering siliciclastics were lithified, before erosional ice advance, and long before significant burial of the Enorama Fm.

4.2. Syn-glacial meteoric diagenesis

Meteoric diagenetic alteration associated with sea level drawdown and subaerial exposure during the Marinoan ice age has been proposed as an origin for the Trezona $\delta^{13}C$ anomaly (Knauth and Kennedy, 2009; Swart and Kennedy, 2012) (Hypothesis 3, Fig. 5a [3]). Flat-topped, shallow-water carbonate platforms can become exposed to $\delta^{13}C$- and $\delta^{18}O$-depleted meteoric water during sea-level fall, leading to depth-dependent variation in $\delta^{13}C$ and $\delta^{18}O$ beneath the subaerial carbonate

exposure surface (Allan and Matthews, 1982). These isotopically-depleted meteoric fluids would become progressively heavier with depth as they mix with relatively isotopically-enriched marine porewaters below the new syn-glacial base level (Allan and Matthews, 1982). Such a trend would be duplicated in altered carbonates, with the most enriched and covarying $\delta^{13}C$–$\delta^{18}O$ near the base of the altered stratigraphy within the meteoric-marine mixing zone (Moore, 2001; Swart and Eberli, 2005) (Fig. 5a [3c]). This pattern is observed in the Clino core of the Great Bahama Bank, which has undergone periodic subaerial exposure during the glacial–interglacial cycles of the Plio-Pleistocene. For a single period of exposure to be sufficient to alter hundreds of meters of stratigraphy, the meteoric influx must be exceptionally ^{13}C-depleted. Terrestrial biomass, with $\delta^{13}C$ values that are >20‰ lower than primary carbonate values, provides the main source of organic matter in the Bahamas, as primary marine organic matter within the carbonates is typically <0.5% (Knauth and Kennedy, 2009).

In general, the Trezona Fm represents a single shoaling upward sequence that lacks evidence for subaerial exposure in either physical or sequence stratigraphic analysis (Figs. 2 and 3). The one exception to this pattern is the impressive glacial erosional surface that truncates the top of the Trezona Fm. Any meteoric alteration along this surface would need to be synchronous with the accumulation of enough land-ice somewhere on the globe to cause sea level to fall and expose the platform, but before local glaciers truncated the $\delta^{13}C$–$\delta^{18}O$ profile on the carbonate platform during deposition of the Elatina Fm (Fig. 5a [3]). In contrast to the Great Bahama Bank data, where the uppermost carbonates record the most negative $\delta^{13}C$ values, the Trezona Fm records a profile with the most depleted and covarying $\delta^{13}C$–$\delta^{18}O$ values near the base of the altered stratigraphy, ~200 m below the truncation surface (Fig. 5a [3]). To create the complete observed Trezona $\delta^{13}C$ profile by meteoric diagenesis would require a sea level drawdown of ~5–200 m, where high freshwater recharge rates and low hydraulic conductivity values for the Trezona carbonates would lead to smaller required sea level drops (Budd and Vacher, 1991) (Fig. 5a [3]). The carbonate reef of the Trezona Fm is approximately 35 km wide and is restricted to the central anticline of the ARC with laterally equivalent silt-dominated facies towards the north and south (Fig. 1). Thus, the resulting freshwater lens could have penetrated ~350 m deep into this paleo-island and generated a marine mixing zone within the organic carbon-rich Enorama shales, leading to highly depleted $\delta^{13}C$ values and $\delta^{13}C$–$\delta^{18}O$ covariation at the base of the Trezona Fm. It is therefore possible that growth of just a Greenland-sized ice sheet somewhere in the world could have stimulated meteoric diagenesis through the entire thickness of the Trezona Fm. However, if such a small sea level change is sufficient for extreme diagenetic alteration of a 300 m thick column of rock, why is such dramatic $\delta^{13}C$ modification not more pervasive in the rock record? The underlying Etina Fm has evidence of periodic exposure, has a similar island geometry, and also is underlain by organic-rich shales and silts of the Tapley Hills Fm, but the $\delta^{13}C$ values remain +10‰. To explain the Trezona anomaly by meteoric diagenesis, one would have to find evidence that the carbonates were particularly disposed to $\delta^{13}C$ alteration, due either to the peculiar nature of their organic carbon content or to the oxidizing power of porewaters at the time (Grotzinger et al., 2011).

Diagenesis models (Hypotheses 1–3) also predict that the severity of physical and isotopic alteration should scale with the permeability and porosity of each unit. Primary porosity and permeability are a function of grain size and shape, degree of sorting, and sedimentation rate indicative of each lithofacies (Beard and Weyl, 1973). Following recrystallization and porosity reduction, the distribution of secondary porosity and permeability is controlled by the original lithofacies because fluid migration still preferentially occurs along grain boundaries (Moore, 2001). Therefore, diagenesis models predict spatially variable, grain size-dependent $\delta^{13}C$ (Fig. 5a [1b, 2b, 3b]). However, Trezona Fm $\delta^{13}C$ and $\delta^{18}O$ show no lithofacies-dependent trends (Fig. 6b, c), and the Trezona $\delta^{13}C$ anomaly is reproducible with minimal scatter at 1 cm, 1 km and 100 km scales, despite being recorded in a wide range of carbonate lithofacies across 45,000 km^2 (Fig. 6a).

4.3. Pre-glacial primary dissolved inorganic carbon

The Trezona $\delta^{13}C$ anomaly could record changes in oceanic DIC at the time of sedimentation (Hypotheses 4–5, Fig. 5a [4], [5]). Similar to South Australia, the Trezona anomaly in northern Namibia spans 30–50 m of predominantly shallow, platform-facies carbonates (Halverson et al., 2002; Miller, 2008). A simple thermal subsidence model accounting for glacial erosion suggested that the start of the negative $\delta^{13}C$ anomaly preceded glacioeustatic sea level fall by ~1 Myr (Halverson et al., 2002; Halverson et al., 2005; Hoffman, 2011) (Hypothesis 5). Ice-rafted debris in the upper Trezona $\delta^{13}C$ recovery requires synchroneity between the recovery of $\delta^{13}C$ to 0‰ and the glaciation (Fig. 5a [5a]. Together, these observations imply that the isotopic nadir predates the growth of significant land ice, but that the Trezona anomaly did not significantly predate glaciation.

5. Conclusions

Does the nadir of the Trezona $\delta^{13}C$ anomaly record a primary signal of global ocean DIC as a cause or a consequence of the transition into low-latitude glaciation, or are the two events completely unrelated? The former hypothesis is favored because a primary DIC origin fails the fewest geological and isotopic tests (Pavlov et al., 2003; Schrag et al., 2002; Swanson-Hysell et al., 2010). To achieve very negative primary $\delta^{13}C$ values below the long-term mantle input (~−6‰), additional inputs of ^{13}C-depleted material are required. Determining the duration of the Trezona $\delta^{13}C$ anomaly (negative shift and recovery) is critical to constraining the size and isotopic composition of the requisite reservoir of light carbon, to differentiate between sources such as methane (Bjerrum and Canfield, 2011; Pavlov et al., 2003; Schrag et al., 2002), dissolved organic carbon (Fike et al., 2006; Rothman et al., 2003; Swanson-Hysell et al., 2010; Tziperman et al., 2011) or remineralized particulate organic matter (Higgins and Schrag, 2006), and to evaluate the influence of such an event on the global carbon cycle and climate.

Sedimentological and geochemical constraints require that the $\delta^{13}C$ anomaly was recorded in carbonate sediments prior to local glacial erosion, thus ruling out any late-stage burial diagenesis hypothesis. While the meteoric diagenesis hypothesis can be made consistent with the new timing constraints presented here, it is inconsistent with the lack of permeability-dependent diagenetic indicators. We favor a primary DIC origin for the $\delta^{13}C$ signal, with the recovery from the global $\delta^{13}C$ Trezona anomaly synchronous with the first debris-laden icebergs in the tropics.

Acknowledgments

Field, stable isotope and geochronology work was supported by NSF grant EAR-0842946 and a Sloan Foundation Research Fellowship awarded to Maloof. We benefited from discussions with Peter Swart. In addition, Meytal Higgins and Judy Swan provided numerous constructive comments on drafts that greatly improved the paper. Fiona Best, Blake Dyer, Ryan Ewing, Brehnin Keller, Justin Strauss, and Nora Xu provided enthusiastic assistance in the field. Darren Crawford gave invaluable help accessing the Flinders Ranges National Park. We are very grateful to the landowners and pastoralists for land access. Claire Calmet, Will Jacobsen, Jacquie Nesbit, Justin Strauss, and Nora Xu helped with sample preparation. Stable isotope measurements were performed at the University of Michigan by Lora Wingate and Kacey Lohmann and at Princeton University. Andrew

Kylander-Clark and Gareth Seward are thanked for assistance with U–/INS;Pb geochronologic analyses at UCSB.

Appendix A. Supplementary data

Supplementary data to this article can be found online at doi:10.1016/j.epsl.2011.12.027.

References

Allan, J., Matthews, R., 1982. Isotope signatures associated with early meteoric diagenesis. Sedimentology 29, 797–817.

Beard, D., Weyl, P., 1973. Influence of texture on porosity and permeability of unconsolidated sand. Bull. Am. Assoc. Pet. Geol. 51, 349–369.

Bjerrum, C., Canfield, D., 2011. Towards a quantitative understanding of the late Neoproterozoic carbon cycle. Proc. Natl. Acad. Sci. 108 (14), 5542–5547.

Budd, D., Vacher, H., 1991. Predicting the thickness of fresh-water lenses in carbonate paleo-islands. J. Sediment. Petrol. 61 (1), 43–53.

Burns, S., Matter, A., 1993. Carbon isotopic record of the latest Proterozoic. Eclogae Geol. Helv. 86 (2), 595–607.

Calver, C., 2000. Isotope stratigraphy of the Ediacaran (Neoproterozoic III) of the Adelaide rift complex, Australia, and the overprint of water column stratification. Precambrian Res. 100, 121–150.

Condon, D., Zhu, M., Bowring, S., Wang, W., Yang, A., Jin, Y., 2005. U–Pb ages from the Neoproterozoic Doushantuo Formation, China. Science 308, 95–98.

Cottle, J., Horstwood, M., Parrish, R., 2009a. A new approach to single shot laser ablation analysis and its application to in situ Pb/U geochronology. J. Anal. At. Spectrom. 24 (10), 1355–1363.

Cottle, J., Jessup, M., Newall, M., Horstwood, M., Noble, S., Parrish, R., Waters, D., Searle, M., 2009b. Geochronology of granulitized eclogite from the Ama Drime Massif: implications for the tectonic evolution of the South Tibetan Himalaya. Tectonics 28 (1), TC1002. doi:10.1029/2008TC002256.

Cottle, J., Searle, M., Horstwood, M., Waters, D.J., 2009c. Timing of Mid-crustal metamorphism, melting and deformation in the Mt. Everest region of southern Tibet revealed by U(−Th)–Pb geochronology. J. Geol. 117 (6), 643–664.

Derry, L., 2010a. A burial diagenesis origin for the Ediacaran Shuram-Wonoka carbon isotope anomaly. Earth Planet. Sci. Lett. 294, 152–162.

Derry, L., 2010b. On the significance of $\delta^{13}C$ correlations in ancient sediments. Earth Planet. Sci. Lett. 296 (3–4), 497–501.

Derry, L., 2010c. Geochemical constraints on the origin of C, O and S isotopic variations in Neoproterozoic carbonates. GSA Denver Annual Meeting 161-16.

Fanning, M., 2006. Constraints on the timing of the Sturtian glaciation from southern Australia; i.e., for the true Sturtian. Geological Society of America Abstracts with Programs., Vol. 38, p. 115.

Fike, D., Grotzinger, J., Pratt, L., Summon, R., 2006. Oxidation of the Ediacaran ocean. Nature 444, 744–747.

Goodge, J., Vervoort, J., Fanning, C., Brecke, D., Farmer, G., Williams, I., Myrow, P., DePaola, D., 2008. A positive test of East Antarctica–Laurentia Juxtaposition within the Rodinia Supercontinent. Science 321, 235–240.

Grotzinger, J., Fike, D., Fischer, W., 2011. Enigmatic origin of the largest-known carbon isotope excursion in Earth's history. Nat. Geosci.. doi:10.1038/NGEO1138.

Halverson, G., Hoffman, P., Schrag, D., 2002. A major perturbation of the carbon cycle before the Ghaub glaciation (Neoproterozoic) in Namibia: prelude to snowball Earth? Geochem. Geophys. Geosyst. 3. doi:10.1029/2001GC000244.

Halverson, G., Hoffman, P., Maloof, A., Schrag, D., Rice, A.H.N., Bowring, S., Dudas, F., 2005. Toward a Neoproterozoic composite carbon-isotope record. Geol. Soc. Am. Bull. 117, 1181–1207.

Higgins, J., Schrag, D., 2006. Beyond methane: towards a theory for the Paleocene-Eocene Thermal Maximum. Earth Planet. Sci. Lett. 245, 523–537.

Hoffman, P., 2011. Strange bedfellows: glacial diamictite and cap carbonate from the Marinoan (635 Ma) glaciation in Nambia. Sedimentology 58, 57–119.

Hoffman, P., Halverson, G., Grotzinger, J., 2002. Are Proterozoic cap carbonates and isotopic excursions a record of gas hydrate destabilization following Earth's coldest intervals?: comment and Reply. Geology 30, 286–287.

Hoffmann, K.-H., Condon, D., Bowring, S., Crowley, J., 2004. A U–Pb zircon date from the Neoproterozoic Ghaub Formation, Namibia: constraints on Marinoan glaciation. Geology 32, 817–820.

Jackson, S., Pearson, N., Griffin, W., Belousova, E., 2004. The application of laser ablation-inductively coupled plasma-mass spectrometry to in situ U/Pb zircon geochronology. Chem. Geol. 657 (211), 47–69.

Karlstrom, K., Bowring, S., 1988. Early Proterozoic assembly of tectonostratigraphic terranes in southwestern North America. J. Geol. 96, 561–576.

Kaufman, A., Knoll, A., Narbonne, G., 1997. Isotopes, ice ages, and terminal Proterozoic Earth history. Proc. Natl. Acad. Sci. 95, 6600–6605.

Kaufman, A., Corsetti, F., Varni, M., 2007. The effect of rising atmospheric oxygen on carbon and sulfur isotope anomalies in the Neoproterozoic Johnnie Formation, Death Valley, USA. Chem. Geol. 237, 47–63.

Knauth, L., Kennedy, M., 2009. The late Precambrian greening of the Earth. Nature 460, 728–732.

Lemon, N., 2000. A Neoproterozoic fringing stromatolite reef complex, Flinders Ranges, South Australia. Precambrian Res. 100, 109–120.

Lemon, N., Gostin, V., 1990. Glacigenic sediments of the late Proterozoic Elatina Formation and equivalents, Adelaide Geosyncline, South Australia. In: Jago, J., Moore, P. (Eds.), The Evolution of a Late Precambrian–Early Palaeozoic Rift Complex: Geological Society of Austalia, Vol. 16, pp. 149–164.

Lewis, K., Keeler, T., Maloof, A., 2011. New software for plotting and analyzing stratigraphic data. EOS Trans. Am. Geophys. Union 92 (5), 37–38.

Li, Z., Bogdanova, S., Collins, A., Davison, A., De Waele, B., Ernst, R., Fitzsimons, I., Fuck, R., Gladkochub, D., Jacobs, J., Karlstrom, K., Lul, S., Natapov, L., Pease, V., Pisarevsky, S., Thrane, K., Vernikovsky, V., 2008. Assembly, configuration, and break-up history of Rodinia: a synthesis. Precambrian Res. 160, 179–210.

Macdonald, F., Schmitz, M., Crowley, J., Roots, C., Jones, D., Maloof, A., Strauss, J., Cohen, P., Johnston, D., Schrag, D., 2010. Calibrating the Cryogenian. Science 327, 1241–1243.

Maloof, A., Rose, C., Beach, R., Samuels, B., Calmet, C., Erwin, D., Poirier, G., Yao, N., Simons, F., 2010. Possible animal-body fossils in pre-Marinoan limestones from South Australia. Nat. Geosci. 3 (9), 653–659.

McFadden, K., Huang, J., Chu, X., Kaufman, A., Zhou, C., Yuan, X., Xiao, S., 2008. Pulsed oxidation and biological evolution in the Ediacaran Doushantuo Formation. Proc. Natl. Acad. Sci. 105 (9), 3197–3202.

McKirdy, D., Burgess, J., Lemon, N., Yu, X., Cooper, A., Gostin, V., Jenkins, R., Both, R., 2001. A chemostratigraphic overview of the late Cryogenian interglacial sequence in the Adelaide Fold-Thrust Belt, South Australia. Precambrian Res. 106, 149–186.

Melezhik, V., Roberts, D., Fallick, A., Gorokhov, I., 2008. The Shuram-Wonoka event recorded in a high-grade metamorphic terrane: insight from the Scandinavian Caledonides. Geol. Mag. 145 (2), 161–172.

Miller, R.M., 2008. The geology of Namibia: Neoproterozoic to Lower Palaeozoic. Geological Survey of Namibia., Vol. 2.

Moore, C., 2001. Carbonate reservoirs: porosity evolution and diagenesis in a sequence stratigraphic framework. Developments in Sedimentology., Vol. 55. Elsevier.

Narbonne, G., Kaufman, A., Knoll, A., 1994. Integrated chemostratigraphy and biostratigraphy of the Windermere Supergroup, northwestern Canada; implications for Neoproterozoic correlations and the early evolution of animals. Geol. Soc. Am. Bull. 106 (10), 1281–1292.

Paton, C., Woodhead, J., Hellstrom, J., Hergt, J., Greig, A., Maas, R., 2010. Improved laser ablation U–Pb zircon geochronology through robust downhole fractionation correction. Geochem. Geophys. Geosyst. 11, Q0AA06.

Pavlov, A., Hurtgen, M., Kasting, J., Arthur, M., 2003. Methane-rich Proterozoic atmosphere. Geology 31 (1), 87–90.

Prave, A., Fallick, A., Thomas, C., Graham, C., 2009. A composite C-isotope profile for the Neoproterozoic Dalradian Supergroup of Scotland and Ireland: implications for global correlations, and timing and duration of deposition. J. Geol. Soc. London 166, 845–857.

Preiss, W., Robertson, R., 2002. South Australian mineral explorers guide. Tech. rep PIRSA.

Rose, C., Maloof, A., 2010. Testing models for post-glacial 'cap dolostone' deposition: Nuccaleena Formation, South Australia. Earth Planet. Sci. Lett. 296, 165–180.

Rothman, D., Hayes, J., Summons, R., 2003. Dynamics of the Neoproterozoic carbon cycle. Proc. Natl. Acad. Sci. 100 (14), 124–129.

Schrag, D., Berner, R., Hoffman, P., Halverson, G., 2002. On the initiation of a snowball Earth. Geochem. Geophys. Geosyst. 300. doi:10.1029/2001GC000219.

Seewald, J., 2003. Organic–inorganic interactions in petroleum-producing sedimentary basins. Nature 426, 327–333.

Sohl, L., Christie-Blick, N., Kent, D., 1999. Paleomagnetic polarity reversals in Marinoan (ca. 600 Ma) glacial deposits of Australia: implications for the duration of low-latitude glaciation in Neoproterozoic time. Geol. Soc. Am. Bull. 111, 1120–1139.

Swanson-Hysell, N., Rose, C., Calmet, C., Halverson, G., Hurtgen, M., Maloof, A., 2010. Cryogenian Glaciation and the onset of carbon-isotope decoupling. Science 328, 608–611.

Swart, P., 2008. Global synchronous changes in the carbon isotopic composition of carbonate sediments unrelated to changes in the global carbon cycle. Proc. Natl. Acad. Sci. 105 (37), 13741–13745.

Swart, P., Eberli, G., 2005. The nature of the $\delta^{13}C$ of periplatform sediments: implications for stratigraphy and the global carbon cycle. Sediment. Geol 175, 115–129.

Swart, P., Kennedy, M., 2012. Does the global stratigraphic reproducibility of δ13C in Neoproterozoic carbonates require a marine origin? A Pliocene-Pleistocene comparison. Geology 40 (1), 87–90.

Tziperman, E., adn Halevy, I., Johnston, D., Knoll, A., Schrag, D., 2011. Biologically induced initiation of Neoproterozoic snowball-Earth events. Proceedings of the National Academy of Sciences.

Wiedenbeck, M., Alle, P., Corfu, F., Griffin, W., Meier, M., Oberli, F., Von Quadt, A., Roddick, J., Spiegel, W., 1995. Three natural zircon standards for U–Th–Pb, Lu–Hf, trace element and REE analyses. Geostand. Newsl. 19 (1), 1–23.

Xiao, S., Bao, H., Wang, H., Kaufman, A., Zhou, C., Li, G., Yuan, X., Ling, H., 2004. The Neoproterozoic Quruqtagh Group in eastern Chinese Tianshan: evidence for a post-Marinoan glaciation. Precambrian Res. 130, 1–26.

Supplementary Online Materials: Constraints on the origin and relative timing of Trezona $\delta^{13}C$ anomaly below the end-Cryogenian glaciation.

Rose, C.V., Swanson-Hysell, N.L., Husson, J., Poppick, L.N., Cottle, J.M., Schoene, B. and Maloof, A.C.

S1 Additional figure

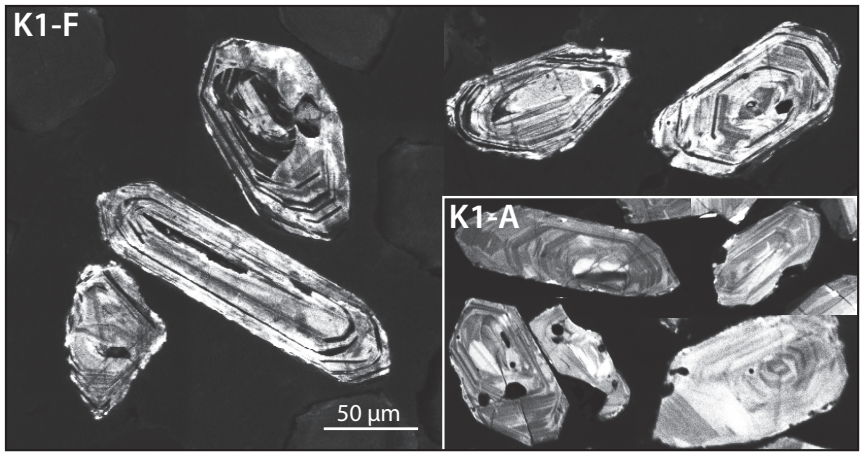

Figure S1. A selection of cathodoluminescence images of zircons with simple concentric zonation from the granite clasts (K1-A and K1-F) within the ice-rafted debris layer in the microbialite bioherm of the Trezona Fm, Punches Rest.

S2 Data

Era	**Fm**	**Section**	**Strat (m)**	**#samples**	δ^{13}**C** range, μ, σ	δ^{18}**O** range, μ, σ	**m** δ^{18}O vs. δ^{13}C, meters vs. δ^{13}C, meters vs. δ^{18}O	**R**^{2}	**p**
Cryogenian	Etina-Trezona	Emu Gap	1176	574			1.35, 0.01, 0.00	0.20	<0.01
		Elatina Creek	575	71			2.25, -0.02, 0.00	0.32	<0.01
		Mooloolloo	1112	314			1.81, -0.01, -0.01	0.21	<0.01
	Etina	Emu Gap	876	354	12.14, 8.02, 1.77	11.07, -8.35, 2.56	0.12, 0.00, -0.01	0.03	<0.01
		Elatina Creek	416	33	4.50, 8.21, 1.12	7.89, -10.16, 1.91	0.24, 0.00, -0.01	0.16	0.02
		Mooloolloo	672	206	5.15, 8.37, 0.93	9.43, -9.80, 1.66	0.07, 0.00, -0.01	0.01	0.09
	Trezona	Emu Gap	300	220	6.88, -6.34, 1.91	5.46, -10.29, 1.29	0.67, 0.03, 0.01	0.21	<0.01
		(δ^{13}C<-7)		93			0.27, 0.01, 0.03	0.36	<0.01
		(δ^{13}C>-7)		127			-0.81, 0.03, -0.01	0.30	<0.01
		Elatina Creek	159	38	8.40, -7.20, 1.93	7.02, -12.27, 1.50	0.29, 0.02, 0.00	0.05	0.17
		(δ^{13}C<-7)		27			0.08, 0.00, 0.01	0.35	0.38
		(δ^{13}C>-7)		11			0.39, 0.00, -0.04	0.36	0.05
		Trezona Bore	261	71	8.82, -6.30, 2.10	6.34, -10.07, 1.14	0.94, 0.02, 0.01	<0.01	0.7
		(δ^{13}C<-7)		28			0.33, 0.01, 0.02	0.43	<0.01
		(δ^{13}C>-7)		43			-1.19, 0.05, 0.00	0.15	0.01
		Mooloolloo	440	108	7.15, -6.02, 1.80	7.14, -11.59, 1.25	0.05, 0.02, 0.00	<0.01	0.7
		(δ^{13}C<-7)		39			0.39, 0.01, 0.02	0.61	<0.01
		(δ^{13}C>-7)		69			-0.47, 0.03, -0.02	0.20	<0.01

Era	Fm	Section	Strat (m)	#samples	$\delta^{13}C$ range, μ, σ	$\delta^{18}O$ range, μ, σ	m $\delta^{18}O$ vs. $\delta^{13}C$, meters vs. $\delta^{13}C$, meters vs. $\delta^{18}O$	R^2	p
Cryogenian *cont.*	Ombaatjie	P4006	197	57	15.00, 1.58, 4.99	11.69, -6.81, 2.72	0.78, -0.06, 0.00	0.18	<0.01
		($\delta^{13}C$<-2.5)		18			0.35, 0.01, 0.08	0.09	0.22
		($\delta^{13}C$>-2.5)		39			0.15, -0.02, 0.04	0.03	0.30
Miocene-	Great Bahama Bank	Clino	299	234	12.4, -0.49, 3.12	7.89, -2.18, 1.86	1.407, -0.034, -0.021	0.706	<0.001
Pleistocene		($\delta^{13}C$<-2.5)		62			-0.53, -0.04, 0.00	0.06	0.06
		($\delta^{13}C$>-2.5)		172			1.13, -0.03, -0.02	0.81	<0.01

Table S1. $\delta^{18}O$-$\delta^{13}C$ statistics for the 'Trezona' $\delta^{13}C$ isotope anomaly in the Cryogenian and the $\delta^{13}C$ record on the Great Bahamas Bank during the Miocene-Pleistocene. Slope (m), R^2 and *p* values have been calculated for the whole section, as well as for $\delta^{13}C$<-2.5 and $\delta^{13}C$>-2.5. Data references: South Australian Etina-Trezona Fms (this paper), Namibian Ombaatjie Fm (Halverson et al., 2005), and Great Bahamas Bank (Swart and Eberli, 2005).

Table S2: U-Pb isotopic data for youngest single zircon grains retrieved from five ice-rafted clasts embedded within stromatolites at the top of the Trezona Fm carbonate platform. All uncertainties are 2σ. % discordance = [($^{207}Pb/^{206}Pb$ - $^{206}Pb/^{238}U$) / $^{207}Pb/^{206}Pb$]×100]

				Isotopic ratios							*Dates (Ma)*				
Sample	**[U] ppm**	**[Pb] ppm**	**[Th]/ [U] ppm**	**$^{206}Pb/^{238}U$**	**% error**	**$^{207}Pb/^{235}U$**	**% error**	**$^{207}Pb/^{206}Pb$**	**% error**	**corr. coef.**	**$^{206}Pb/^{238}U$**	**±**	**$^{207}Pb/^{206}Pb$**	**±**	**% discordance**
K1-A	199	82	0.45	0.32922	1.33	4.94634	1.54	0.10948	1.30	0.98	1834.08	21.34	1790.85	23.62	-2.41
	120	73	0.76	0.31504	1.57	4.60338	1.70	0.10601	1.31	0.98	1764.84	24.23	1731.88	24.10	-1.90
	121	70	0.71	0.31081	1.06	4.71072	1.22	0.10980	1.29	0.92	1744.52	16.24	1796.17	23.47	2.88
	134	67	0.59	0.30326	1.19	4.52929	1.42	0.10873	1.32	0.94	1707.15	17.87	1778.19	24.13	4.00
	167	115	0.96	0.30414	1.19	4.45563	1.28	0.10721	1.33	0.96	1713.75	17.46	1752.46	24.27	2.21
	137	81	0.64	0.30426	1.62	4.51399	1.60	0.10841	1.32	0.99	1711.69	24.36	1772.87	24.03	3.45
	197	118	0.77	0.31034	1.21	4.59748	1.37	0.10840	1.29	0.98	1742.05	18.53	1772.76	23.60	1.73
	108	64	0.75	0.31479	1.83	4.62886	1.96	0.10689	1.30	0.98	1763.34	28.32	1747.02	23.73	-0.93
	172	100	0.65	0.31356	1.34	4.65502	1.43	0.10854	1.30	0.99	1757.71	20.57	1775.03	23.65	0.98
	292	257	1.05	0.31326	1.62	4.58615	1.66	0.10644	1.30	0.99	1759.26	24.38	1739.40	23.84	-1.14
	132	82	0.69	0.31542	1.54	4.70213	1.58	0.10833	1.30	0.99	1766.63	23.74	1771.54	23.66	0.28
	129	67	0.62	0.31518	2.13	4.59397	2.35	0.10587	1.34	0.98	1764.94	32.91	1729.46	24.54	-2.05
	112	56	0.55	0.32231	1.97	4.80037	2.05	0.10784	1.34	0.98	1799.83	30.92	1763.23	24.56	-2.08
	262	164	0.74	0.31560	1.14	4.64099	1.30	0.10767	1.32	0.94	1767.90	17.63	1760.28	24.10	-0.43
	191	187	1.11	0.31924	1.38	4.79802	1.51	0.10799	1.31	0.98	1785.55	21.58	1765.73	23.86	-1.12
	127	58	0.55	0.31873	1.83	4.63899	1.94	0.10572	1.32	0.99	1782.63	28.43	1726.92	24.25	-3.23
	192	167	1.02	0.31896	1.52	4.73627	1.49	0.10775	1.31	0.97	1783.93	23.72	1761.65	23.86	-1.26
	118	68	0.65	0.31812	1.64	4.74074	1.69	0.10814	1.34	0.95	1779.88	25.47	1768.35	24.53	-0.65

Table S2 – Continued

				Isotopic ratios							*Dates (Ma)*				
Sample	**[U] ppm**	**[Pb] ppm**	**[Th]/ [U] ppm**	**^{206}Pb/ ^{238}U**	**% error**	**^{207}Pb/ ^{235}U**	**% error**	**^{207}Pb/ ^{206}Pb**	**% error**	**corr. coef.**	**^{206}Pb/ ^{238}U**	**±**	**^{207}Pb/ ^{206}Pb**	**±**	**% discordance**
K1-A	130	70	0.60	0.31822	1.73	4.75266	1.79	0.10829	1.29	0.99	1780.20	26.91	1770.83	23.53	-0.53
(contd.)	208	171	0.89	0.31766	1.50	4.75232	1.66	0.10882	1.27	0.99	1777.64	23.33	1779.83	23.10	0.12
	235	169	0.82	0.31989	1.67	4.77143	1.79	0.10817	1.29	0.99	1788.43	26.06	1768.77	23.62	-1.11
	290	179	0.70	0.32038	1.15	4.74454	1.37	0.10807	1.31	0.97	1791.24	18.00	1767.19	23.96	-1.36
	155	100	0.72	0.32170	1.56	4.81165	1.64	0.10844	1.27	0.99	1797.29	24.60	1773.37	23.25	-1.35
	267	144	0.65	0.31557	1.11	4.62334	1.30	0.10701	1.30	0.98	1767.77	17.20	1749.08	23.79	-1.07
	112	53	0.58	0.31881	1.72	4.63710	1.87	0.10543	1.33	0.98	1783.24	26.77	1721.86	24.49	-3.56
	141	83	0.66	0.32129	1.41	4.75322	1.63	0.10784	1.34	0.96	1795.50	22.17	1763.23	24.43	-1.83
	125	58	0.53	0.31964	1.32	4.73839	1.38	0.10765	1.32	0.94	1787.49	20.65	1760.01	24.20	-1.56
	101	57	0.60	0.32109	1.27	4.79511	1.39	0.10871	1.33	0.98	1794.58	19.89	1777.95	24.33	-0.94
	143	76	0.56	0.32004	1.45	4.80702	1.51	0.10905	1.34	0.97	1789.32	22.67	1783.60	24.44	-0.32
	177	104	0.63	0.31854	1.28	4.77819	1.41	0.10931	1.29	0.98	1782.14	19.97	1787.88	23.56	0.32
	176	91	0.55	0.31842	1.58	4.77635	1.60	0.10906	1.32	0.96	1781.25	24.55	1783.85	24.10	0.15
	179	99	0.62	0.32858	1.29	4.91725	1.44	0.10788	1.32	0.96	1830.99	20.53	1763.93	24.09	-3.80
	223	124	0.61	0.32343	1.33	4.85435	1.39	0.10895	1.29	0.99	1805.93	21.01	1782.00	23.43	-1.34
	140	89	0.68	0.32647	1.35	5.00259	1.64	0.11162	1.54	0.94	1820.71	21.32	1826.04	28.00	0.29
	138	84	0.68	0.31913	1.28	4.72476	1.40	0.10735	1.30	0.98	1785.01	20.00	1754.97	23.75	-1.71
	224	205	1.07	0.31875	1.53	4.75733	1.58	0.10797	1.28	0.99	1782.91	23.84	1765.51	23.37	-0.99
	146	94	0.70	0.32060	1.84	4.78254	1.95	0.10832	1.32	0.98	1791.68	28.72	1771.43	24.14	-1.14
	142	79	0.61	0.32174	1.47	4.81757	1.50	0.10866	1.32	0.98	1797.55	23.13	1777.00	24.05	-1.16
	193	95	0.56	0.32171	1.47	4.73134	1.58	0.10742	1.31	0.98	1797.48	23.14	1756.14	24.01	-2.35
	173	104	0.64	0.32087	1.67	4.81548	1.73	0.10867	1.32	0.98	1793.12	26.25	1777.27	24.11	-0.89
	162	100	0.73	0.31839	1.35	4.68832	1.50	0.10705	1.33	0.95	1784.15	21.48	1749.79	24.31	-1.96

Table S2 – Continued

				Isotopic ratios							*Dates (Ma)*				
Sample	**[U] ppm**	**[Pb] ppm**	**[Th]/ [U] ppm**	**^{206}Pb/ ^{238}U**	**% error**	**^{207}Pb/ ^{235}U**	**% error**	**^{207}Pb/ ^{206}Pb**	**% error**	**corr. coef.**	**^{206}Pb/ ^{238}U**	**±**	**^{207}Pb/ ^{206}Pb**	**±**	**% discordance**
K1-A	110	44	0.47	0.31866	1.17	4.67347	1.45	0.10699	1.35	0.93	1782.86	18.16	1748.77	24.68	-1.95
(contd.)	161	95	0.65	0.32147	1.56	4.79661	1.77	0.10783	1.32	0.98	1796.26	24.39	1763.03	24.19	-1.88
	110	68	0.68	0.32091	1.35	4.77194	1.30	0.10808	1.35	0.98	1793.62	21.11	1767.36	24.62	-1.49
	122	64	0.55	0.32119	1.68	4.95494	1.98	0.11171	1.56	0.95	1794.84	26.38	1827.40	28.37	1.78
	153	85	0.66	0.31780	1.32	4.62656	1.35	0.10638	1.32	0.97	1778.53	20.41	1738.38	24.25	-2.31
	141	88	0.68	0.32056	1.34	4.79240	1.38	0.10879	1.29	0.98	1791.92	21.01	1779.24	23.55	-0.71
	157	94	0.64	0.31992	1.60	4.78787	1.63	0.10924	1.30	0.99	1788.57	25.00	1786.74	23.69	-0.10
	145	96	0.76	0.32031	1.63	4.73493	1.65	0.10753	1.32	0.98	1790.52	25.55	1758.01	24.15	-1.85
	162	99	0.68	0.32074	1.64	4.81355	1.67	0.10895	1.32	0.99	1792.51	25.62	1781.99	24.10	-0.59
	200	122	0.67	0.32138	1.31	4.82877	1.44	0.10898	1.30	0.97	1795.97	20.50	1782.45	23.69	-0.76
	178	99	0.63	0.32097	1.51	4.80806	1.70	0.10762	1.32	0.97	1797.14	24.27	1759.46	24.14	-2.14
	291	157	0.65	0.32160	1.48	4.71730	1.65	0.10762	1.30	0.99	1796.99	23.18	1759.45	23.80	-2.13
	125	64	0.55	0.32072	1.38	4.79196	1.49	0.10875	1.34	0.97	1795.77	22.06	1778.67	24.47	-0.96
	161	107	0.78	0.32073	1.54	4.69745	1.61	0.10739	1.30	0.99	1792.60	24.19	1755.53	23.85	-2.11
	157	83	0.65	0.31785	1.40	4.61987	1.64	0.10632	1.33	0.98	1778.73	21.89	1737.30	24.33	-2.38
	146	93	0.75	0.31595	2.13	4.57437	2.30	0.10547	1.33	0.99	1768.75	32.82	1722.61	24.36	-2.68
	124	68	0.60	0.32194	1.82	4.84172	1.94	0.10783	1.32	0.97	1798.32	28.62	1763.08	24.19	-2.00
	152	94	0.67	0.32215	1.20	4.81288	1.19	0.10847	1.29	0.98	1799.80	18.87	1773.91	23.62	-1.46
	176	99	0.62	0.32135	1.47	4.76187	1.59	0.10777	1.33	0.97	1800.18	21.48	1762.03	24.24	-2.17
	107	59	0.58	0.32227	1.52	4.80398	1.60	0.10868	1.34	0.98	1800.07	23.92	1777.34	24.42	-1.28
	109	58	0.63	0.31754	1.32	4.72572	1.47	0.10769	1.34	0.98	1782.75	21.38	1760.74	24.43	-1.25
	160	93	0.62	0.32995	1.55	4.92765	1.57	0.10859	1.29	0.99	1837.39	24.87	1775.83	23.57	-3.47
	120	72	0.67	0.32387	1.25	4.81218	1.33	0.10771	1.38	0.97	1811.11	20.35	1761.00	25.26	-2.85

Table S2 – Continued

				Isotopic ratios							*Dates (Ma)*				
Sample	**[U] ppm**	**[Pb] ppm**	**[Th]/ [U] ppm**	**^{206}Pb/ ^{238}U**	**% error**	**^{207}Pb/ ^{235}U**	**% error**	**^{207}Pb/ ^{206}Pb**	**% error**	**corr. coef.**	**^{206}Pb/ ^{238}U**	**±**	**^{207}Pb/ ^{206}Pb**	**±**	**% discordance**
K1-A	143	81	0.66	0.31966	1.24	4.68723	1.36	0.10740	1.33	0.96	1790.25	19.94	1755.75	24.38	-1.96
(contd.)	284	230	0.93	0.32158	1.42	4.84026	1.51	0.10947	1.30	0.96	1796.88	22.27	1790.63	23.68	-0.35
	190	140	0.82	0.32945	1.69	4.91476	1.72	0.10806	1.31	0.99	1834.83	26.97	1766.95	23.96	-3.84
	153	90	0.63	0.32159	1.32	4.79920	1.39	0.10912	1.29	0.99	1797.00	20.62	1784.86	23.60	-0.68
	171	95	0.64	0.32008	1.07	4.68602	1.20	0.10705	1.31	0.95	1789.86	16.67	1749.78	24.06	-2.29
	134	81	0.68	0.32463	1.30	4.86417	1.27	0.10857	1.31	0.98	1811.76	20.49	1775.48	23.89	-2.04
	109	123	1.23	0.32278	1.14	4.79057	1.27	0.10749	1.39	0.96	1802.91	18.00	1757.24	25.50	-2.60
	151	97	0.67	0.32295	1.57	4.83900	1.70	0.10888	1.30	0.98	1803.39	24.80	1780.70	23.80	-1.27
	97	52	0.58	0.32292	1.40	4.84361	1.62	0.10886	1.38	0.97	1803.40	22.08	1780.48	25.12	-1.29
	172	102	0.67	0.32385	1.45	4.76797	1.53	0.10775	1.32	0.97	1807.93	22.81	1761.70	24.20	-2.62
	151	102	0.75	0.32143	1.22	4.80015	1.39	0.10836	1.32	0.98	1799.08	19.69	1771.97	24.19	-1.53
	151	95	0.71	0.32168	1.05	4.79615	1.18	0.10781	1.33	0.95	1797.63	16.39	1762.66	24.32	-1.98
	153	90	0.65	0.32236	1.43	4.83943	1.58	0.10846	1.30	0.98	1800.61	22.46	1773.75	23.67	-1.51
	90	47	0.57	0.32191	1.16	4.75576	1.29	0.10716	1.36	0.98	1798.68	18.19	1751.76	24.95	-2.68
	132	80	0.66	0.32471	1.64	4.84276	1.65	0.10802	1.32	0.99	1811.90	25.79	1766.37	24.14	-2.58
	190	174	1.02	0.32394	1.40	4.79437	1.48	0.10787	1.31	0.98	1808.40	22.16	1763.82	23.96	-2.53
	115	67	0.64	0.32412	1.67	4.82528	1.75	0.10735	1.33	0.97	1809.07	26.32	1754.89	24.40	-3.09
	128	61	0.50	0.32309	1.91	4.84528	2.07	0.10907	1.36	0.97	1803.72	30.12	1784.03	24.75	-1.10
	138	79	0.62	0.32626	1.41	4.87381	1.50	0.10885	1.32	0.97	1819.62	22.41	1780.27	24.01	-2.21
	206	130	0.75	0.32187	1.26	4.71762	1.36	0.10743	1.30	0.98	1798.45	19.81	1756.29	23.85	-2.40
	156	113	0.78	0.32374	1.65	4.86160	1.71	0.10886	1.31	0.99	1810.63	25.42	1780.51	23.87	-1.69
	121	78	0.72	0.32222	1.40	4.78505	1.49	0.10771	1.34	0.98	1799.95	21.97	1761.06	24.52	-2.21
	139	77	0.62	0.32315	1.15	4.74859	1.30	0.10769	1.34	0.94	1804.79	18.09	1760.73	24.47	-2.50

Table S2 – Continued

				Isotopic ratios							*Dates (Ma)*				
Sample	**[U] ppm**	**[Pb] ppm**	**[Th]/ [U] ppm**	**^{206}Pb/ ^{238}U**	**% error**	**^{207}Pb/ ^{235}U**	**% error**	**^{207}Pb/ ^{206}Pb**	**% error**	**corr. coef.**	**^{206}Pb/ ^{238}U**	**±**	**^{207}Pb/ ^{206}Pb**	**±**	**% discordance**
K1-A	174	115	0.70	0.32092	1.33	4.82799	1.53	0.10887	1.30	0.95	1797.47	21.88	1780.64	23.72	-0.95
(contd.)	128	71	0.60	0.32249	1.40	4.81019	1.45	0.10851	1.35	0.98	1801.28	21.99	1774.61	24.65	-1.50
	97	48	0.54	0.32373	1.43	4.83730	1.52	0.10833	1.38	0.96	1807.26	22.55	1771.58	25.23	-2.01
	125	73	0.65	0.32443	1.39	4.85291	1.50	0.10805	1.34	0.98	1810.77	21.98	1766.84	24.43	-2.49
	148	79	0.59	0.32285	1.37	4.74518	1.48	0.10740	1.33	0.97	1805.87	22.05	1755.85	24.31	-2.85
	173	115	0.74	0.32633	1.24	4.85825	1.35	0.10805	1.30	0.94	1820.10	19.72	1766.82	23.76	-3.02
	234	145	0.72	0.32370	1.15	4.81627	1.23	0.10780	1.29	0.98	1807.39	18.13	1762.51	23.56	-2.55
	110	53	0.53	0.32275	1.61	4.78571	1.71	0.10779	1.33	0.97	1802.48	25.25	1762.47	24.33	-2.27
	130	72	0.60	0.32521	1.31	4.85276	1.48	0.10817	1.31	0.97	1814.61	20.73	1768.91	23.98	-2.58
	145	77	0.57	0.32642	1.46	4.90553	1.56	0.10926	1.31	0.99	1820.40	23.13	1787.08	23.90	-1.86
	128	65	0.56	0.32557	1.63	4.79401	1.65	0.10767	1.33	0.97	1816.12	25.76	1760.43	24.37	-3.16
	178	111	0.69	0.32482	1.56	4.78626	1.70	0.10770	1.32	0.98	1812.55	24.59	1760.83	24.10	-2.94
	121	72	0.64	0.32599	1.59	4.87750	1.62	0.10870	1.32	0.98	1818.14	25.15	1777.76	23.99	-2.27
	187	104	0.59	0.32592	1.26	4.88658	1.34	0.10931	1.28	0.96	1818.09	20.00	1787.90	23.34	-1.69
	107	58	0.62	0.32313	1.94	4.80974	2.11	0.10750	1.31	0.99	1803.98	30.71	1757.53	24.02	-2.64
	130	64	0.56	0.32372	1.52	4.74740	1.73	0.10756	1.33	0.97	1807.22	23.96	1758.49	24.31	-2.77
K1-B	110	124	2.01	0.19286	1.58	2.08517	3.14	0.07788	2.64	0.89	1136.70	16.46	1143.94	52.43	0.63
	172	73	0.68	0.21084	1.53	2.36188	2.79	0.08063	2.51	0.95	1233.10	17.13	1212.50	49.40	-1.70
	129	43	0.53	0.21157	1.55	2.33562	2.86	0.07956	2.54	0.94	1236.98	17.38	1186.01	50.24	-4.30
	177	101	0.61	0.31791	1.32	4.74379	1.78	0.10822	1.83	0.98	1779.12	20.54	1769.70	33.47	-0.53
K1-C	110	53	0.61	0.32434	1.12	4.92994	1.31	0.11031	0.88	0.95	1810.49	17.75	1804.54	16.00	-0.33

Table S2 – Continued

				Isotopic ratios							*Dates (Ma)*				
Sample	**[U] ppm**	**[Pb] ppm**	**[Th]/ [U] ppm**	**^{206}Pb/ ^{238}U**	**% error**	**^{207}Pb/ ^{235}U**	**% error**	**^{207}Pb/ ^{206}Pb**	**% error**	**corr. coef.**	**^{206}Pb/ ^{238}U**	**±**	**^{207}Pb/ ^{206}Pb**	**±**	**% discordance**
K1-C	133	140	1.36	0.30335	1.57	4.35831	1.62	0.10399	0.91	0.98	1711.25	24.44	1696.59	16.68	-0.86
(contd.)	260	158	0.80	0.30753	1.34	4.49240	1.53	0.10622	0.87	0.98	1728.01	20.29	1735.57	15.99	0.44
K1-F	192	94	0.58	0.30908	1.21	4.59823	1.51	0.10727	0.88	0.99	1735.79	18.45	1753.63	16.04	1.02
	201	106	0.65	0.31773	1.27	4.70262	1.52	0.10664	0.90	0.97	1780.87	20.16	1742.82	16.47	-2.18
	178	131	0.89	0.31863	1.18	4.71466	1.50	0.10736	0.89	0.98	1785.27	18.85	1755.03	16.28	-1.72
	184	147	0.95	0.32025	1.59	4.74415	1.73	0.10763	0.89	0.99	1790.23	24.91	1759.73	16.33	-1.73
	186	158	1.13	0.30728	1.08	4.52645	1.36	0.10712	0.89	0.97	1727.04	16.36	1751.06	16.31	1.37
	151	158	1.41	0.32036	1.51	5.09037	1.62	0.11573	0.85	0.98	1790.85	23.63	1891.30	15.31	5.31
	195	127	0.79	0.31917	1.43	4.70890	1.65	0.10765	0.90	0.98	1785.06	22.34	1760.08	16.38	-1.42
	151	74	0.58	0.32080	1.30	4.74124	1.48	0.10797	0.90	0.97	1793.19	20.30	1765.38	16.51	-1.58
	160	173	1.32	0.31493	1.22	4.64781	1.50	0.10801	0.90	0.98	1764.56	18.91	1766.21	16.45	0.09
	244	199	1.00	0.30466	1.29	4.52086	1.48	0.10861	0.88	0.99	1713.93	19.42	1776.17	16.14	3.50
	154	83	0.66	0.31783	1.32	4.72446	1.54	0.10820	0.90	0.98	1778.68	20.49	1769.37	16.51	-0.53
	144	100	0.85	0.31829	1.21	4.73581	1.45	0.10862	0.90	0.98	1780.98	18.79	1776.43	16.48	-0.26
	188	102	0.65	0.32091	1.20	4.78351	1.45	0.10879	0.88	0.98	1793.76	18.83	1779.32	16.11	-0.81
	175	161	1.12	0.31406	1.69	4.76419	1.87	0.11082	0.90	0.96	1759.86	26.04	1812.93	16.27	2.93
	152	76	0.58	0.30156	2.20	4.51395	2.09	0.10938	0.95	0.99	1702.18	33.72	1789.05	17.34	4.86
	154	350	2.74	0.31918	1.35	4.75716	1.53	0.10853	0.88	0.98	1785.20	21.09	1774.87	16.05	-0.58
	265	193	0.90	0.30676	1.10	4.58550	1.34	0.10862	0.88	0.98	1726.74	17.11	1776.44	16.09	2.80
	122	80	0.78	0.30917	1.26	4.62004	1.50	0.10871	0.89	0.97	1736.25	19.07	1777.97	16.29	2.35
	115	114	1.16	0.31892	0.57	4.76425	0.94	0.10831	0.90	0.85	1784.38	8.92	1771.15	16.40	-0.75
	184	189	1.18	0.31188	0.80	4.73286	1.05	0.10990	0.90	0.85	1749.82	12.25	1797.82	16.44	2.67

Table S2 – Continued

				Isotopic ratios								*Dates (Ma)*				
Sample	**[U] ppm**	**[Pb] ppm**	**[Th]/ [U] ppm**	**^{206}Pb/ ^{238}U**	**% error**	**^{207}Pb/ ^{235}U**	**% error**	**^{207}Pb/ ^{206}Pb**	**% error**	**corr. coef.**	**^{206}Pb/ ^{238}U**	**±**	**^{207}Pb/ ^{206}Pb**	**±**	**% discordance**
K1-F	147	44	0.34	0.32255	0.67	4.82711	1.01	0.10845	0.88	0.93	1803.28	10.74	1773.56	16.11	-1.68
(contd.)	156	106	0.81	0.31319	0.79	4.64051	1.13	0.10723	0.91	0.93	1756.25	12.21	1752.82	16.57	-0.20
	96	43	0.53	0.30466	0.74	4.54765	1.15	0.10815	0.93	0.86	1714.28	11.08	1768.49	16.93	3.07
	176	158	1.05	0.31808	0.88	4.75093	1.23	0.10823	0.89	0.95	1780.13	13.72	1769.90	16.32	-0.58
	164	107	0.74	0.32360	0.68	4.91476	1.05	0.10956	0.87	0.95	1807.16	10.76	1792.13	15.81	-0.84
	226	127	0.68	0.31052	0.81	4.64523	1.10	0.10812	0.88	0.96	1743.11	12.36	1768.03	16.00	1.41
	161	267	2.13	0.30392	1.04	4.50758	1.12	0.10679	0.95	0.86	1710.43	15.63	1745.28	17.33	2.00
	99	72	0.83	0.32473	1.06	4.75935	1.08	0.10630	0.86	0.95	1812.48	16.71	1736.92	15.73	-4.35
	82	37	0.64	0.31390	0.98	4.64691	1.04	0.10750	0.88	0.90	1759.60	15.04	1757.53	16.07	-0.12
	156	190	1.43	0.31790	1.01	4.71196	1.04	0.10744	0.85	0.96	1779.20	15.70	1756.47	15.56	-1.29
	144	105	0.84	0.31834	1.02	4.74885	1.18	0.10855	0.85	0.96	1781.32	15.80	1775.15	15.51	-0.35
	202	127	0.75	0.31113	1.06	4.58756	1.13	0.10684	0.83	0.98	1745.97	16.18	1746.25	15.24	0.02
	129	91	0.80	0.32262	1.15	4.79049	1.13	0.10777	0.87	0.95	1802.13	18.05	1762.10	15.94	-2.27
	233	160	0.81	0.31508	1.23	4.67820	1.32	0.10756	0.83	0.98	1765.23	18.97	1758.42	15.11	-0.39
	254	73	0.34	0.32090	1.06	5.04077	1.05	0.11390	0.78	0.98	1793.80	16.60	1862.56	14.09	3.69
	259	181	0.81	0.31348	1.44	4.69853	1.50	0.10833	0.82	0.99	1760.47	21.42	1771.57	14.99	0.63
	180	128	0.82	0.31601	1.34	4.71398	1.29	0.10839	0.83	0.98	1772.95	21.57	1772.55	15.20	-0.02
	119	137	1.35	0.31660	1.06	4.70772	1.14	0.10813	0.85	0.96	1772.79	16.40	1768.22	15.47	-0.26
	105	90	1.00	0.32411	1.15	4.83591	1.20	0.10804	0.85	0.96	1811.80	17.67	1766.58	15.55	-2.56
	139	44	0.37	0.31819	1.04	4.78367	1.05	0.10904	0.83	0.97	1780.56	16.13	1783.52	15.17	0.17
	193	89	0.57	0.30287	1.94	4.50904	2.05	0.10777	0.84	0.99	1704.55	29.35	1762.14	15.38	3.27
	256	146	0.68	0.30668	1.05	4.61310	1.13	0.10881	0.82	0.99	1724.09	15.98	1779.61	14.99	3.12
	124	83	0.77	0.31373	1.31	4.67936	1.45	0.10800	0.88	0.98	1758.54	20.19	1766.00	16.07	0.42

Table S2 – Continued

				Isotopic ratios							*Dates (Ma)*				
Sample	**[U] ppm**	**[Pb] ppm**	**[Th]/ [U] ppm**	**^{206}Pb/ ^{238}U**	**% error**	**^{207}Pb/ ^{235}U**	**% error**	**^{207}Pb/ ^{206}Pb**	**% error**	**corr. coef.**	**^{206}Pb/ ^{238}U**	**±**	**^{207}Pb/ ^{206}Pb**	**±**	**% discordance**
K1-F	140	83	0.67	0.32209	1.50	4.79192	1.64	0.10778	0.88	0.99	1799.24	23.52	1762.18	16.08	-2.10
(contd.)	187	169	1.04	0.31050	1.60	4.69572	1.63	0.10971	0.85	0.99	1742.41	24.46	1794.58	15.47	2.91
	199	100	0.55	0.31965	1.45	4.97517	1.57	0.11279	0.83	0.99	1790.77	21.99	1844.92	14.94	2.94
	173	141	0.85	0.33214	1.86	5.11593	1.99	0.11152	0.86	0.98	1847.63	29.85	1824.27	15.64	-1.28
	143	66	0.50	0.30675	1.50	4.60980	1.65	0.10857	0.87	0.99	1727.63	23.42	1775.54	15.81	2.70
	291	176	0.69	0.30988	1.38	4.66042	1.52	0.10928	0.85	0.99	1739.54	21.05	1787.37	15.40	2.68
	178	118	0.73	0.31821	1.44	4.77451	1.56	0.10887	0.88	0.98	1783.60	22.92	1780.56	16.13	-0.17
	191	150	0.90	0.30886	1.34	4.66170	1.50	0.10951	0.85	0.99	1734.61	20.29	1791.29	15.53	3.16
	191	179	1.12	0.30362	1.37	4.52159	1.50	0.10782	0.88	0.98	1708.76	20.53	1762.83	16.03	3.07
	107	75	0.78	0.32656	1.86	4.82849	1.99	0.10801	0.89	0.99	1820.63	29.41	1766.16	16.34	-3.08
	265	205	0.89	0.31478	1.41	4.73772	1.56	0.10911	0.85	0.99	1763.62	21.77	1784.66	15.50	1.18
	245	87	0.39	0.30912	1.21	4.61571	1.33	0.10846	0.85	0.99	1735.97	18.32	1773.78	15.52	2.13
	182	93	0.57	0.30458	1.78	4.63205	1.93	0.11011	0.86	0.99	1713.11	26.76	1801.28	15.62	4.90
	149	129	1.06	0.31537	1.22	4.83114	1.32	0.11139	0.85	0.97	1766.64	18.80	1822.25	15.40	3.05
K1-G	263	77	0.55	0.21220	1.47	2.30529	1.90	0.07909	1.18	0.97	1240.18	16.61	1174.38	23.44	-5.60
	81	52	1.23	0.21629	2.20	2.38281	2.60	0.08051	1.28	0.96	1261.44	25.18	1209.49	25.30	-4.30
	81	61	1.45	0.20586	2.24	2.27700	2.74	0.07949	1.32	0.95	1205.97	24.62	1184.25	26.03	-1.83
	296	21	0.15	0.18015	1.34	1.83734	2.10	0.07396	1.27	0.96	1067.57	13.23	1040.26	25.59	-2.63
	347	83	0.55	0.16694	2.03	1.68018	2.68	0.07296	1.31	0.97	994.81	18.74	1012.96	26.50	1.79
	49	16	0.67	0.18848	1.73	1.98647	2.35	0.07715	1.40	0.92	1112.73	17.68	1125.01	27.98	1.09

References

Halverson, G., Hoffman, P., Maloof, A., Schrag, D., Rice, A. H. N., Bowring, S., Dudas, F., 2005. Toward a Neoproterozoic composite carbon-isotope record. Geological Society of America Bulletin 117, 1181–1207.

Swart, P., Eberli, G., 2005. The nature of the δ^{13}c of periplatform sediments: Implications for stratigraphy and the global carbon cycle. Sedimentary Geology 175, 115–129.